CALCIUM SIGNALING

A single amino acid deletion in the ER Ca^{2+} sensor STIM1 reverses the in vitro and in vivo effects of the Stormorken syndrome–causing R304W mutation

Thilini H. Gamage[1]†‡, Herwig Grabmayr[2]†, Ferdinand Horvath[3]†, Marc Fahrner[2], Doriana Misceo[1], William Edward Louch[4], Gjermund Gunnes[5], Helen Pullisaar[6]§, Janne Elin Reseland[6], Staale Petter Lyngstadaas[6], Asbjørn Holmgren[1], Silja S. Amundsen[1], Petr Rathner[7,8], Linda Cerofolini[9], Enrico Ravera[9,10], Heinrich Krobath[3], Claudio Luchinat[10,11], Thomas Renger[3], Norbert Müller[7,12,13], Christoph Romanin[2]||*, Eirik Frengen[1]||*

Stormorken syndrome is a multiorgan hereditary disease caused by dysfunction of the endoplasmic reticulum (ER) Ca^{2+} sensor protein STIM1, which forms the Ca^{2+} release–activated Ca^{2+} (CRAC) channel together with the plasma membrane channel Orai1. ER Ca^{2+} store depletion activates STIM1 by releasing the intramolecular "clamp" formed between the coiled coil 1 (CC1) and CC3 domains of the protein, enabling the C terminus to extend and interact with Orai1. The most frequently occurring mutation in patients with Stormorken syndrome is R304W, which destabilizes and extends the STIM1 C terminus independently of ER Ca^{2+} store depletion, causing constitutive binding to Orai1 and CRAC channel activation. We found that in cis deletion of one amino acid residue, Glu^{296} (which we called E296del) reversed the pathological effects of R304W. Homozygous Stim1 E296del+R304W mice were viable and phenotypically indistinguishable from wild-type mice. NMR spectroscopy, molecular dynamics simulations, and cellular experiments revealed that although the R304W mutation prevented CC1 from interacting with CC3, the additional deletion of Glu^{296} opposed this effect by enabling CC1-CC3 binding and restoring the CC domain interactions within STIM1 that are critical for proper CRAC channel function. Our results provide insight into the activation mechanism of STIM1 by clarifying the molecular basis of mutation-elicited protein dysfunction and pathophysiology.

INTRODUCTION

Store-operated Ca^{2+} entry (SOCE) is a critical Ca^{2+}-regulating pathway in eukaryotic cells. Stromal interaction molecule 1 (STIM1) in the endoplasmic reticulum (ER) and ORAI calcium release–activated calcium modulator 1 (Orai1) in the plasma membrane (PM) form the Ca^{2+} release–activated Ca^{2+} (CRAC) channel machinery, which facilitates SOCE (*1*, *2*). STIM1 is a ubiquitously expressed, highly conserved, single-pass transmembrane (TM) protein that spans the ER membrane, with the N-terminal region located in the ER lumen and the C-terminal region located in the cytosol (fig. S1A). The N-terminal EF-hand binds to Ca^{2+} and is therefore a sensor for the ER luminal Ca^{2+} level (*3*, *4*). The STIM1 C-terminal region contains three coiled-coil domains (CC1, CC2, and CC3) (*1*, *5*–*9*), which collectively represent the Orai-activating small fragment (OASF). The coiled-coil 1 domain (CC1) contains the helices CC1α1, CC1α2, and CC1α3. In the inactive state, when the ER is Ca^{2+} replete, direct CC1α1-CC3 interactions act as a clamp to hold STIM1 in its tight, quiescent conformation (*10*–*12*). Upon ER store depletion, Ca^{2+} detaches from the EF-hand, initiating the activation process of the protein (*1*, *2*, *4*). The activation signal propagates over the TM domain and results in CC1α1 dimerization, in which an intermediate CC1α1-CC1α2 interaction may occur (*13*), supporting the release of the CC1α1-CC3 clamp. Last, STIM1 reaches the activated fully extended conformation (*5*, *6*, *11*, *13*, *14*). Activated STIM1 further translocates toward ER-PM junctions (*4*, *5*, *11*). The extended conformation of STIM1 exposes the CRAC-activating domain (CAD), also known as the STIM1-Orai1–activating region (SOAR), which is mainly composed of CC2-CC3, for interaction with Orai1 (*11*, *13*, *15*, *16*). STIM1 and Orai1 together form a highly specialized CRAC channel, in which Orai1 acts as the pore-forming subunit and facilitates Ca^{2+} entry across the PM (*17*, *18*).

Mutations in either component of the CRAC channel may result in loss or gain of CRAC channel activity (*6*). Both gain-of-function and loss-of-function mutations in CRAC channel components

[1]Department of Medical Genetics, Oslo University Hospital and University of Oslo, 0450 Oslo, Norway. [2]Institute of Biophysics, Johannes Kepler University Linz, Gruberstrasse 40, 4020 Linz, Austria. [3]Institute of Theoretical Physics, Johannes Kepler University Linz, Altenbergerstrasse 69, 4040 Linz, Austria. [4]Institute for Experimental Medical Research, Oslo University Hospital and University of Oslo, 0450 Oslo, Norway. [5]Faculty of Veterinary Medicine, Norwegian University of Life Sciences, 1430 Ås, Norway. [6]Department of Biomaterials, Institute of Clinical Dentistry, University of Oslo, 0455 Oslo, Norway. [7]Institute of Organic Chemistry and Institute of Inorganic Chemistry, Johannes Kepler University Linz, Altenbergerstrasse 69, 4040 Linz, Austria. [8]Institut für Analytische Chemie, University of Vienna, Währinger Straße 38, 1090 Wien, Austria. [9]Magnetic Resonance Center, University of Florence and Consorzio Interuniversitario Risonanze Magnetiche di Metalloproteine, 50019 Sesto Fiorentino, Italy. [10]Department of Chemistry, Ugo Schiff, University of Florence, 50019 Sesto Fiorentino, Italy. [11]CERM, University of Florence, 50019 Sesto Fiorentino, Italy. [12]Department of Chemistry, Faculty of Science, University of South Bohemia, Branišovská 1645/31A, 370 05 České Budějovice, Czech Republic. [13]Institute of Biochemistry, Johannes Kepler University Linz, Altenbergerstrasse 69, 4040 Linz, Austria.
*Corresponding author. Email: eirik.frengen@medisin.uio.no (E.F.); christoph.romanin@jku.at (C.R.)
†These authors contributed equally to this work.
‡Present address: Institute for Surgical Research, Oslo University Hospital, 0372 Oslo, Norway.
§Present address: Department of Orthodontics, Institute of Clinical Dentistry, University of Oslo, 0455 Oslo, Norway.
||These authors contributed equally to this work.

cause Mendelian diseases (*19*–*21*). Loss-of-function mutations in *STIM1* cause autosomal recessive immunodeficiency [IMD10; Online Mendelian Inheritance in Man (OMIM) #612783] (*21*–*24*). Gain-of-function mutations cause an autosomal dominant clinical continuum ranging from isolated tubular aggregate myopathy (TAM1; OMIM #160565) (*25*) to Stormorken syndrome (STRMK; OMIM #185070), which affects several organs. Patients with Stormorken syndrome present with thrombocytopenia, anemia, tubular aggregate myopathy, muscle fatigue, asplenia/hyposplenia, miosis, migraine, dyslexia, and ichthyosis (*26*–*33*). The most frequent STIM1 gain-of-function mutation reported is R304W, which constitutively activates STIM1 due to an extended conformation of the mutant protein (*6*), resulting in Stormorken syndrome (*28*–*30*). The tryptophan residue at the end of CC1α2 in STIM1 R304W causes an extended α helix with greater rigidity, leading to a tension-induced conformational change between CC1α2-CC1α3 and an increased propensity for CC1 dimerization (*6*, *13*). These effects extend the STIM1 cytosolic region irrespective of ER Ca^{2+} content, thus resulting in gain of function for STIM1. The stabilized extended conformation of STIM1 R304W exposes CAD for interaction with Orai1, resulting in constitutive STIM1-Orai1 binding, which in turn leads to constitutive CRAC channel activation and SOCE (*6*, *12*).

We previously described a mouse line expressing the STIM1 R304W mutant (*34*, *35*). An additional mouse line expressing the same mutation was also reported (*36*). In a homozygous state, both mouse lines presented with perinatal lethality, spleen and hematological anomalies, severe skeletal muscle degeneration, and abnormal bone architecture (*34*–*36*). Here, we present a mouse line ($Stim1^{E296del+R304W}$) expressing two STIM1 mutations in cis, the R304W mutation and deletion of Glu^{296} (which we called E296del), both located in the STIM1 CC1α2 domain. This double mutation has not been previously described in patients. We demonstrated that the additional E296del mutation reverted the pathogenic effects caused by STIM1 R304W. The homozygous double-mutant mice showed normal viability and did not have skeletal muscle or bone pathology. Human embryonic kidney (HEK) 293 cells expressing STIM1 E296del+R304W exhibited store-operated currents similar to those in cells expressing STIM1 wild type (WT). Förster resonance energy transfer (FRET) studies further showed that deletion of Glu^{296} restored a tight conformation reminiscent of inactive STIM1, as opposed to the extended conformation of STIM1 R304W. Multidimensional nuclear magnetic resonance (NMR) spectroscopy and molecular dynamics (MD) simulations showed that the linker between CC1α2 and CC1α3, which is rendered rigid by the R304W mutation (*6*), recovered STIM1 WT-like flexibility when the R304W and E296del mutations were combined. Further, MD simulations and FRET sensor measurements indicated that this deletion resulted in weakened CC1α1-CC1α2 interactions. In the competition between CC1α2 and CC3 for binding to CC1α1, the deletion of Glu^{296} favored the formation of the CC1α1-CC3 clamp, thereby resulting in the quiescent state of STIM1 E296del+R304W.

RESULTS

Generation of the $Stim1^{E296del+R304W}$ mouse line

A *Stim1* knock-in mouse line was established with zinc finger nuclease (ZFN)–induced modification, yielding a total of 144 offspring. Genomic analysis of the target region in the offspring identified two mice with the *Stim1* (NC_000073.6): g.102421471A>T;p.R304W (GRCm38.p6/mm10) mutation only (*34*), and the third carried an additional 3–base pair (bp) deletion in cis: *Stim1* (NC_000073.6): g.102421448-102421450delAAG (GRCm38.p6/mm10), resulting in an in-frame deletion of Glu^{296}, p.E296del. The deletion likely resulted from nonhomologous end-joining, which is an error-prone repair mechanism (*37*), repairing the ZFN-generated double-strand break. This paper focuses on the double-mutant mouse (which we named $Stim1^{E296del+R304W}$). The deletion and the in cis single–base pair substitution in *Stim1* were confirmed by Sanger sequencing. Whole-genome sequencing of DNA from the founder mouse did not detect off-target insertions of the ZFN template and confirmed the *Stim1* (NC_000073.6): g.102421448-102421450delAAG; g.102421471A>T mutations. Sanger sequencing of whole-blood RNA-derived complementary DNA from homozygous $Stim1^{E296del+R304W}$ mice confirmed the expression of the double-mutant allele (fig. S1B).

The $Stim1^{E296del+R304W}$ mouse line exhibited normal Mendelian birth ratio and normal growth

The birth ratio in our $Stim1^{R304W}$ mouse line deviated substantially from the expected Mendelian ratio due to perinatal lethality in homozygotes (*34*). In contrast, 15 heterozygous $Stim1^{E296del+R304W}$ crosses resulted in 102 mice with a birth ratio of 23 (WT):55 (heterozygous $Stim1^{E296del+R304W}$):24 (homozygous $Stim1^{E296del+R304W}$), in agreement with the expected Mendelian ratio of 1:2:1 for crosses between two heterozygotes. Furthermore, crossing of homozygous $Stim1^{E296del+R304W}$ mice resulted in normal litter sizes with viable offspring. Homozygous $Stim1^{E296del+R304W}$ mice exhibited body size, weight, and growth similar to those of WT littermates, further indicating normal viability and development of the double-mutant mice (Fig. 1, A and B). Both heterozygous and homozygous $Stim1^{E296del+R304W}$ mice lived up to 5 to 6 months of age until euthanasia, in contrast to $Stim1^{R304W}$ mice, of which the homozygotes show perinatal lethality with decreased weight and body size in the survivors (*34*).

The $Stim1^{E296del+R304W}$ mouse line displayed normal endurance and skeletal muscle histology

The homozygous $Stim1^{R304W}$ mice show reduced endurance on a treadmill (*34*). The heterozygous and homozygous $Stim1^{E296del+R304W}$ mice, however, presented with treadmill performance similar to that in age-matched WT littermates, as measured by the distance run before exhaustion (Fig. 1C). Thus, the reduced endurance of homozygous $Stim1^{R304W}$ mice (Fig. 1C) (*34*) was rescued in the double-mutant homozygous $Stim1^{E296del+R304W}$ mice. We previously documented reduced muscle mass and severe skeletal muscle degeneration in $Stim1^{R304W}$ mice (*34*). However, skeletal muscle mass was visibly larger in homozygous $Stim1^{E296del+R304W}$ mice than in homozygous $Stim1^{R304W}$ mice (Fig. 1D), which show reduced skeletal muscle mass compared with age- and gender-matched WT littermates (*34*). In addition, the severe skeletal muscle degeneration detected in heterozygous and homozygous $Stim1^{R304W}$ mice—as shown by variation in muscle fiber size, loss of striation, hyper-eosinophilia, increased centralized nuclei, and signs of inflammation (*34*)—was not evident in hematoxylin and eosin (H&E)–stained sections of quadriceps muscle in homozygous $Stim1^{E296del+R304W}$ mice (Fig. 1E).

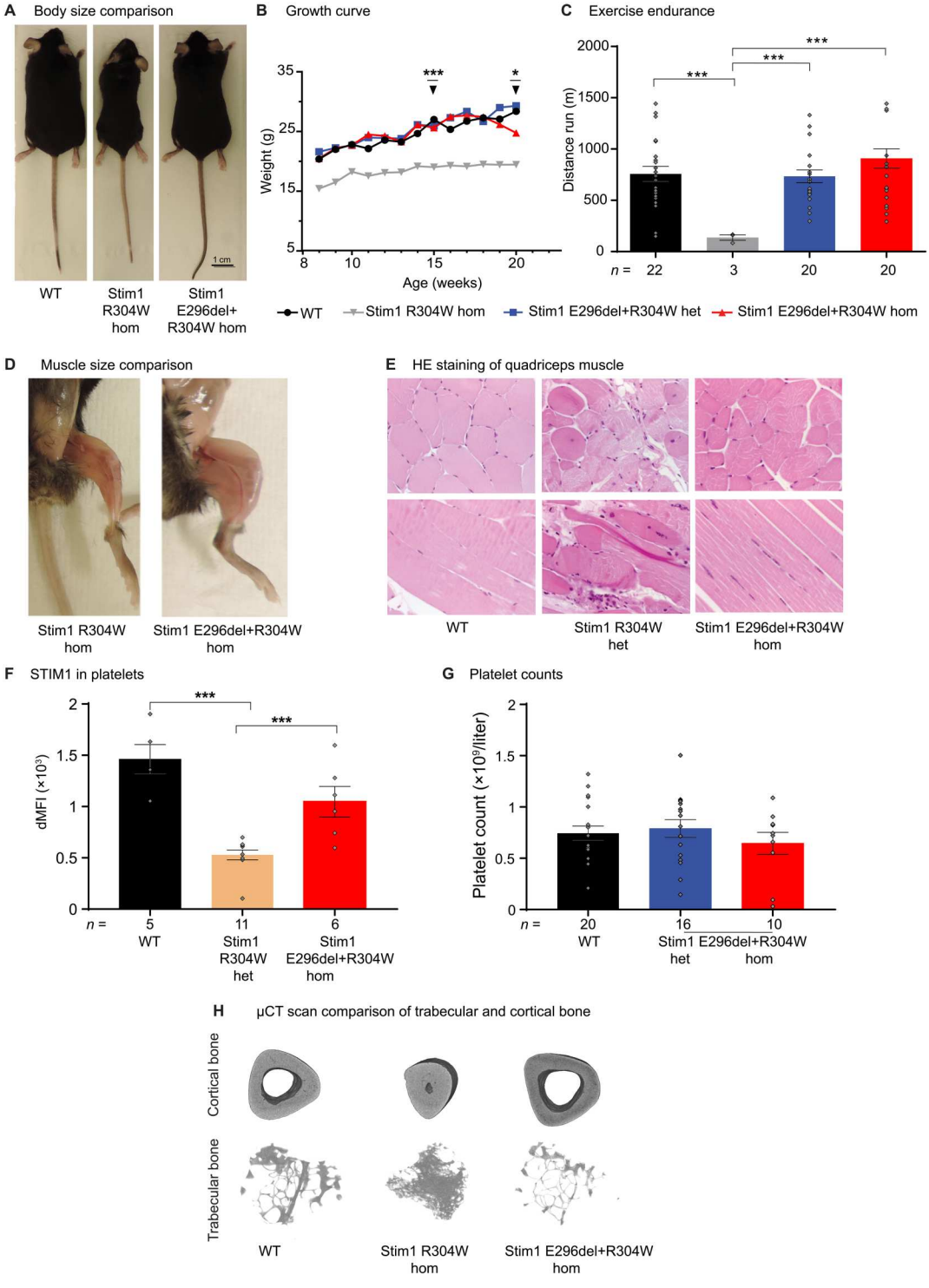

Fig. 1. Phenotypic characterization of Stim1$^{E296del+R304W}$ mice. (**A**) Body size of homozygous (hom) Stim1^{R304W}, Stim1$^{E296del+R304W}$, and WT mice at 20 weeks of age. (**B**) Representative growth curves of mice from all four genotypes. Data points are from female animals ($n = 2$ to 16) and represent the mean weight. Mean weight of homozygous Stim1^{R304W} ($n = 3$) and homozygous Stim1$^{E296del+R304W}$ ($n = 9$) compared at 15 weeks of age ***$P < 0.005$ and homozygous Stim1^{R304W} ($n = 3$) and homozygous Stim1$^{E296del+R304W}$ ($n = 3$) compared at 20 weeks of age; *$P < 0.05$, Student's t test. het, heterozygous. (**C**) Exercise endurance on treadmill in WT ($n = 22$), homozygous Stim1^{R304W} ($n = 3$), heterozygous Stim1$^{E296del+R304W}$ ($n = 20$), and homozygous Stim1$^{E296del+R304W}$ ($n = 20$) animals. ***$P < 0.005$ with Mann-Whitney U test. (**D**) Hind limb muscle mass in 20-week-old homozygous Stim1$^{E296del+R304W}$ mice compared with age- and gender-matched homozygous Stim1^{R304W} mice. Images are representative of $n \geq 3$ mice per group. (**E**) Cross-sections and longitudinal sections of H&E-stained quadriceps muscles from WT, heterozygous Stim1^{R304W}, and homozygous Stim1$^{E296del+R304W}$ mice. Images are representative of $n \geq 3$ mice per group. (**F**) Flow cytometry analysis of STIM1 protein levels in heterozygous Stim1^{R304W} ($n = 11$), homozygous Stim1$^{E296del+R304W}$ ($n = 6$), and WT ($n = 5$) platelets. ***$P < 0.005$ with Mann-Whitney U test. dMFI, relative mean fluorescence intensity. (**G**) Platelet counts in adult WT ($n = 20$), heterozygous ($n = 16$), and homozygous ($n = 10$) Stim1$^{E296del+R304W}$ mice. (**H**) Three-dimensional illustration of the µCT data from cortical and trabecular bone WT, homozygous Stim1^{R304W}, and homozygous Stim1$^{E296del+R304W}$ mice. Images are representative of $n \geq 3$ mice per group. Data represent mean values ± SEM.

These results showed that deletion of Glu^{296} in STIM1 in Stim1$^{E296del+R304W}$ mice prevented the severe skeletal muscle pathology caused by the STIM1 R304W gain-of-function mutation.

Normal abundance of the double-mutant STIM1 protein in Stim1$^{E296del+R304W}$ platelets

STIM1 abundance is reduced in heterozygous Stim1^{R304W} platelets and is undetectable in homozygous Stim1^{R304W} platelets and embryonic liver megakaryocytes (*34*). We confirmed that STIM1 levels in heterozygous Stim1^{R304W} platelets were significantly lower than those in WT platelets (Fig. 1F). However, STIM1

levels in homozygous Stim1$^{E296del+R304W}$ platelets were similar to those in WT platelets and significantly greater than those in heterozygous Stim1^{R304W} platelets (Fig. 1F). Heterozygous and homozygous Stim1$^{E296del+R304W}$ mice also showed average platelet counts in a similar range as WT animals (Fig. 1G). These data demonstrated that the reduction of platelet STIM1 expression in Stim1^{R304W} mice (*34*) was rescued in Stim1$^{E296del+R304W}$ mice.

Stim1$^{E296del+R304W}$ mice showed normal bone architecture

Homozygous Stim1^{R304W} mice have abnormal bone architecture on micro–computed tomography (μCT) scan of the tibia (*35*)—specifically decreased cortical bone area, volume, and surface area; increased trabecular bone volume fraction and trabecular number; and decreased trabecular separation (*35*). Tibia μCT scans revealed similar bone parameters in homozygous Stim1$^{E296del+R304W}$ and WT mice and an absence of the bone anomalies observed in Stim1^{R304W} mice (Fig. 1H and fig. S2). These results demonstrated that in cis E296del deletion rescued the pathological effect of the R304W mutation in bone tissue.

E296del reverted the constitutive activation of STIM1 R304W in HEK293 cells

We next performed whole-cell patch-clamp electrophysiology experiments to track the current density of Orai1 over time in HEK293 cells coexpressing N-terminally tagged cyan fluorescent protein (CFP)–STIM1 and yellow fluorescent protein (YFP)–Orai1. The current density of cells expressing Orai1 with STIM1 WT was 0 at the start of the recording and gradually increased as more Orai1 channels were activated by STIM1 upon passive ER Ca^{2+} store depletion with 20 mM EGTA (Fig. 2A). Cells expressing Orai1 with STIM1 R304W showed maximally activated Orai1 channels irrespective of the ER Ca^{2+} level, which yielded comparable Orai1 current densities at the start and the end of the patch-clamp recordings. In contrast, cells expressing Orai1 with the STIM1 E296del+R304W double mutant showed significantly reduced constitutive Orai1 activation compared with cells expressing STIM1 R304W (Fig. 2A). Although Ca^{2+} store dependence of Orai1 current activation was restored in cells expressing STIM1 E296del+R304W, a small amount of constitutive activity remained. The effects of E296del on STIM1 R304W could also be replicated by deleting the neighboring residues Gln^{295}, Ala^{297}, or Gln^{298} or by inserting an additional alanine between Glu^{296} and Ala^{297}. STIM1 Q295del+R304W, A297del+R304W, Q298del+R304W, and E296_A297insA+R304W all induced store-dependent Orai1 activation similar to STIM1 E296del+R304W (fig. S3, A to C). The STIM1 single-deletion mutants (E296del, Q295del, and A297del) induced store-dependent activation of Orai1 currents to a similar extent as STIM1 WT (Fig. 2A and fig. S3, A and B). Deletion of Gly^{306} or Thr^{307} downstream of Trp^{304} did not replicate the effects of E296del on STIM1 R304W. Similar to STIM1 R304W, STIM1 G306del+R304W and T307del+R304W activated Orai1 channels irrespective of the ER Ca^{2+} level (fig. S3C). We also tested the effect of E296del on other STIM1 gain-of-function mutations L251S and L416S+L423S (*11*), but E296del did not restore these STIM1 mutants to WT behavior (fig. S4A).

In summary, our patch-clamp recordings revealed that deletion of Glu^{296} counteracted the functional effects of the R304W mutation in STIM1. Furthermore, the deletion of not only Glu^{296} but also Gln^{295}, Ala^{297}, or Gln^{298} and insertion of an additional alanine between Glu^{296} and Ala^{297} reduced constitutive Orai1 current density, suggesting that the local effects of these individual amino acids are not critical to counteract the effect of STIM1 R304W. The lack of effects for deletion of Gly^{306} and Thr^{307} indicated that mutations of positions upstream, but not downstream, of Trp^{304} can reverse the constitutive activation of STIM1 R304W.

E296del restored store-dependent STIM1 R304W homomerization and interaction with Orai1

We next carried out intermolecular FRET experiments to independently corroborate the results of our patch-clamp recordings. We measured FRET efficiency (E_{app}) in time course experiments in HEK293 cells coexpressing N-terminal CFP-STIM1 and YFP-STIM1 constructs. After ER Ca^{2+} store depletion by a SERCA inhibitor [thapsigargin (TG)], intermolecular E_{app} for STIM1 WT rose (Fig. 2B) due to the increasing homomerization of activated STIM1. On the other hand, STIM1 R304W showed no FRET increase in response to Ca^{2+} store depletion and was already maximally activated (Fig. 2B), which is in line with the strong constitutive Orai1 activity observed in patch-clamp experiments. As expected, STIM1 E296del+R304W showed a FRET increase similar to that of STIM1 WT, indicating that activation depended on the ER Ca^{2+} store (Fig. 2B). The initial, small FRET efficiency of the STIM1 E296del+R304W double mutant was slightly higher than that of STIM1 WT (Fig. 2B), which was consistent with the small amount of constitutive Orai1 activity with the STIM1 double mutant seen in patch-clamp experiments (Fig. 2A). In addition, confocal fluorescence microscopic CFP/YFP image overlays of resting (before Ca^{2+} store depletion) cells revealed the presence of large STIM1 R304W clusters close to the PM (fig. S4B, left). This contrasted with the sporadic clustering of STIM1 E296del+R304W, which is reminiscent of that of STIM1 WT (fig. S4B, left).

We also performed intermolecular FRET time course experiments using HEK293 cells coexpressing C-terminally tagged STIM1-CFP and Orai1-YFP constructs. TG perfusion resulted in an increase in intermolecular E_{app} in cells expressing STIM1 WT and Orai1, representing the store depletion–induced association between these two proteins (Fig. 2C). Although interaction between STIM1 R304W and Orai1 was already maximal before ER Ca^{2+} store depletion, STIM1 E296del+R304W interacted with Orai1 in an ER Ca^{2+} store–dependent manner. similar to STIM1 WT (Fig. 2C). The FRET efficiency baseline of the double mutant was again slightly elevated, which is in line with both the patch-clamp experiments and FRET analysis of STIM1 homomerization. Last, confocal fluorescence microscopic CFP/YFP image overlays of resting cells showed colocalization of STIM1 R304W with Orai1 in puncta structures within ER-PM junctional regions. STIM1 E296del+R304W was also coclustered with Orai1 in puncta but to a much lesser degree than STIM1 R304W and, again, more reminiscent of STIM1 WT (fig. S4B, right). In summary, results from the intermolecular FRET time course experiments were consistent with the functional electrophysiological results.

A tight state of the STIM1 OASF R304W conformational sensor is restored by E296del

To correlate STIM1 activation states with conformational rearrangements in the STIM1 cytosolic portion, we performed intramolecular FRET experiments using the double fluorescently labeled,

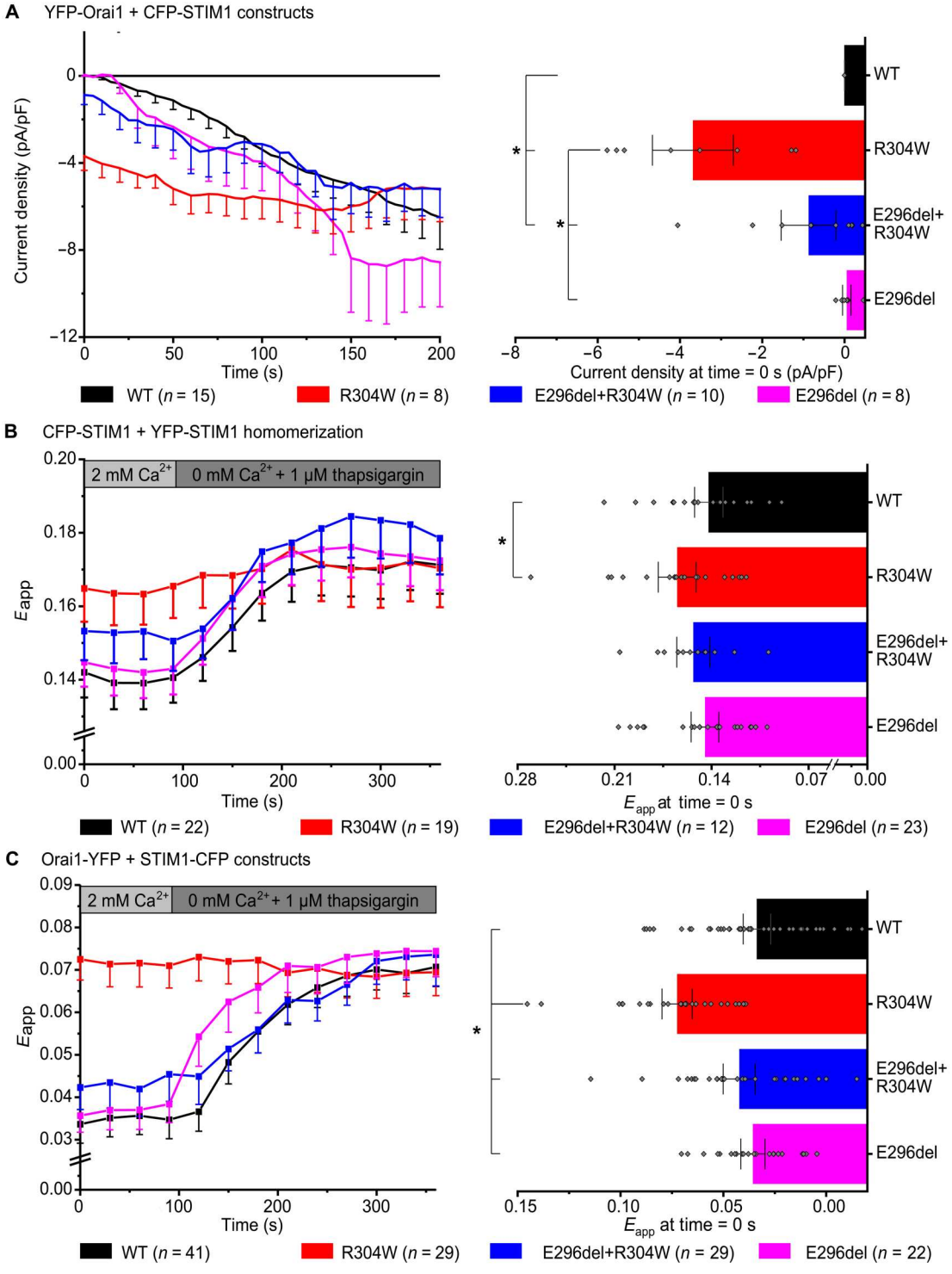

Fig. 2. Patch-clamp electrophysiology and FRET microscopy of STIM1 E296del+R304W. (**A**) Patch-clamp whole-cell recordings of N-terminally tagged YFP-Orai1 coexpressed with N-terminally tagged CFP-STIM1 E296del ± R304W (left) in HEK293 cells and the corresponding initial current density amplitudes in pA/pF (right). (**B** and **C**) Analysis of the changes in intermolecular FRET efficiency (E_{app}) elicited by ER Ca^{2+} store depletion with 1 μM TG (left) in HEK293 cells expressing the indicated constructs and the corresponding initial E_{app} values (right). Homomerization of N-terminally tagged CFP-/YFP-STIM1 E296del ± R304W (B). Interaction of C-terminally tagged STIM1-CFP E296del ± R304W with C-terminally tagged Orai1-YFP (C). Color code: WT (black), R304W (red), E296del+R304W (blue), and E296del (magenta). *$P < 0.05$ by Student's *t* test. Experiments were replicated on at least two different days using independent transfections with the indicated number of cells (*n*). Data represent mean values ± SEM.

soluble C-terminal Orai1-activating small fragment OASF (amino acids 233 to 474, including CC1, CC2, and CC3 domains) of STIM1 as a conformational sensor (YFP-OASF-CFP; Fig. 3A) (*11*). Whereas YFP-OASF-CFP WT exhibited high intramolecular E_{app} consistent with the tight state of quiescent STIM1 (*5*, *11*), the STIM1 R304W mutation switched the conformational sensor into an extended, activated state that was characterized by significantly decreased intramolecular E_{app} (Fig. 3B) (*6*). The double mutant YFP-OASF-CFP E296del+R304W, however, exhibited significantly increased E_{app} in comparison with the YFP-OASF-CFP R304W mutant. The addition of the E296del mutation to the YFP-OASF-CFP R304W mutant thus appeared to reestablish a conformational state that resulted in FRET efficiency levels closer to those of YFP-OASF-CFP WT (Fig. 3B). The lower FRET efficiency of the OASF double mutant compared with WT likely reflects the slight basal activation of the STIM1 double mutant as shown with the functional results presented above.

We also coexpressed the double-labeled YFP-OASF-CFP constructs with unlabeled Orai1 to study their behavior in the presence of the ion channel. Our previous study revealed a significant decrease in FRET efficiency of OASF WT when associated with Orai1 in the PM compared with OASF WT in the cytosolic fraction (*11*), indicating conformational extension upon OASF WT interaction with and activation of Orai1 (fig. S4C). Such a switch was not detected for OASF R304W, presumably because it is in an extended state in the absence and the presence of Orai1 (fig. S4C). Last, similar to OASF WT, YFP-OASF-CFP E296del+R304W underwent a conformational switch into an extended state for the Orai1 PM-associated fraction (fig. S4C).

Deletion of the neighboring residues Gln^{295}, Ala^{297}, or Gln^{298} or insertion of an additional alanine between Glu^{296} and Ala^{297} (Q295del+R304W, A297del+R304W, Q298del+R304W, or E296_A297insA+R304W) in OASF R304W phenocopied the effect of E296del (Fig. 3B and fig. S3, D to F). In contrast, deletion of Gly^{306} or Thr^{307} downstream of Trp^{304} in OASF R304W did not lead to an increase in FRET efficiency comparable to that of E296del. Both YFP-OASF-CFP G306del+R304W and T307del+R304W showed a significant decrease of intramolecular E_{app} with respect to YFP-OASF-CFP WT that was comparable to YFP-OASF-CFP R304W (fig. S3F). Combining E296del with the STIM1 gain-of-function mutations L251S and L416S+L423S (*11*) in OASF resulted in both fragments adopting the same extended states, as signified by low E_{app} values, with and without the deletion of Glu^{296} (fig. S4D).

These intramolecular FRET experiments demonstrated that E296del, Q295del, A297del, Q298del, or insertion of an additional alanine between Glu^{296} and Ala^{297}, but not G306del or T307del, elicited conformational rearrangements in the OASF R304W domain that corresponded to the effect of the mutations in the full-length STIM1 R304W protein. Therefore, Glu^{296} deletion antagonizes the activating effect of the R304W mutation primarily within the OASF domain itself. It does not counteract the activating effect of other gain-of-function mutations such as L251S or L416S+L423S.

E296del reduces the homomerization of the STIM1 CC1 R304W fragment

To further pinpoint the mechanism of action of STIM1 E296del on R304W, we used our FRET-derived interactions in a restricted environment (FIRE) method (*5*) with STIM1 CC1 (233 to 343) constructs (Fig. 3C). The FRET (E_{app}) detectable between CFP-CC1 WT and YFP-CC1 WT reflects the dimerization propensity that is a key step in the process of STIM1 activation (*14*). As published previously, the STIM1 R304W mutation significantly enhanced the homomerization tendency of CC1, as shown by an increase in E_{app} (*6*) (Fig. 3D). The homomerization of CC1 E296del+R304W was similar to that of CC1 WT (Fig. 3D), suggesting that E296del directly counteracted a molecular mechanism induced by this Stormorken syndrome–associated mutation (*6*) by reducing the extent of CC1 homomerization back to that seen in the WT protein, consequently permitting STIM1 to assume a quiescent, tight state despite the presence of the R304W mutation. Thus, these FIRE results provide crucial insights into the mechanism of action of E296del and furthermore allowed us to pinpoint the STIM1 CC1 domain as the relevant region of the protein.

E296del diminishes the rigidity of $loop_2$ located downstream of STIM1 R304W in the CC1α2 helix

Besides the increased tendency of STIM1 CC1 homomerization, another structural effect of the R304W mutation is the increased rigidity of the extended $loop_2$ (which refers to the amino acid stretch after R304W) (fig. S1A) that links the CC1α2 and CC1α3 helices (*6*, *13*). To investigate effects of E296del on the extended $loop_2$ stretch corresponding to CC1 residues Gly^{305}-Ser^{315}, we used comparative NMR relaxation studies. The CC1 E296del+R304W fragment was uniformly labeled at ^{15}N and ^{13}C with C─H random deuteration (^{2}H is about 70%) and purified (*38*). Longitudinal (R_1) and transverse (R_2) relaxation rates of peptide bond ^{15}N atoms provide sequence-specific protein backbone mobility profiles, where higher R_1/R_2 ratios indicate greater mobility (*39*). The STIM1 R304W mutation substantially increases the rigidity of the amino acid backbone immediately after the mutation (*13*). Here, we found that the deletion of Glu^{296}, which is about two helix turns upstream from the R304W mutation, partially restored the mobility of CC1 residues Gly^{305}-Ser^{315}, leading to local mobilities between those of WT and the R304W mutant (Fig. 4A). The restoration of the mobility of $loop_2$ was corroborated by MD simulations comparing the CC1 WT, R304W, and E296del+R304W mutants (Fig. 4B). In these simulations, the difference in the flexibility of $loop_2$ was traced back to the altered electrostatic properties of residue 304 caused by the mutation. The positive charge of Arg^{304} affected the conformation of $loop_2$, with electrostatic interactions preventing $loop_2$ from settling into a rigid helix (fig. S5). In the R304W mutant, the hydrophobic Trp^{304} barely interacted with $loop_2$. The importance of the charge in position 304 was further supported by an in silico experiment artificially neutralizing Arg^{304}, which enabled part of $loop_2$ to settle into a helix (fig. S6). Further, MD simulations using enhanced sampling methods reinforced the reduced mobility of Trp^{304} in the CC1 R304W mutant (fig. S7) (*40*) and the increased helical propensity within CC1α2 and $loop_2$ in the R304W mutant compared with CC1 WT and CC1 E296del+R304W (figs. S8 and S9).

Combining E296del with R304W weakens STIM1 CC1α1-CC1α2 interactions

In NMR spectra of the STIM1 R304W mutants, severe spectral overlap did not allow us to assign the relevant nuclear Overhauser effect contacts of Trp^{304} unequivocally. Therefore, to identify potential interacting residues, we used MD simulations. We compared the

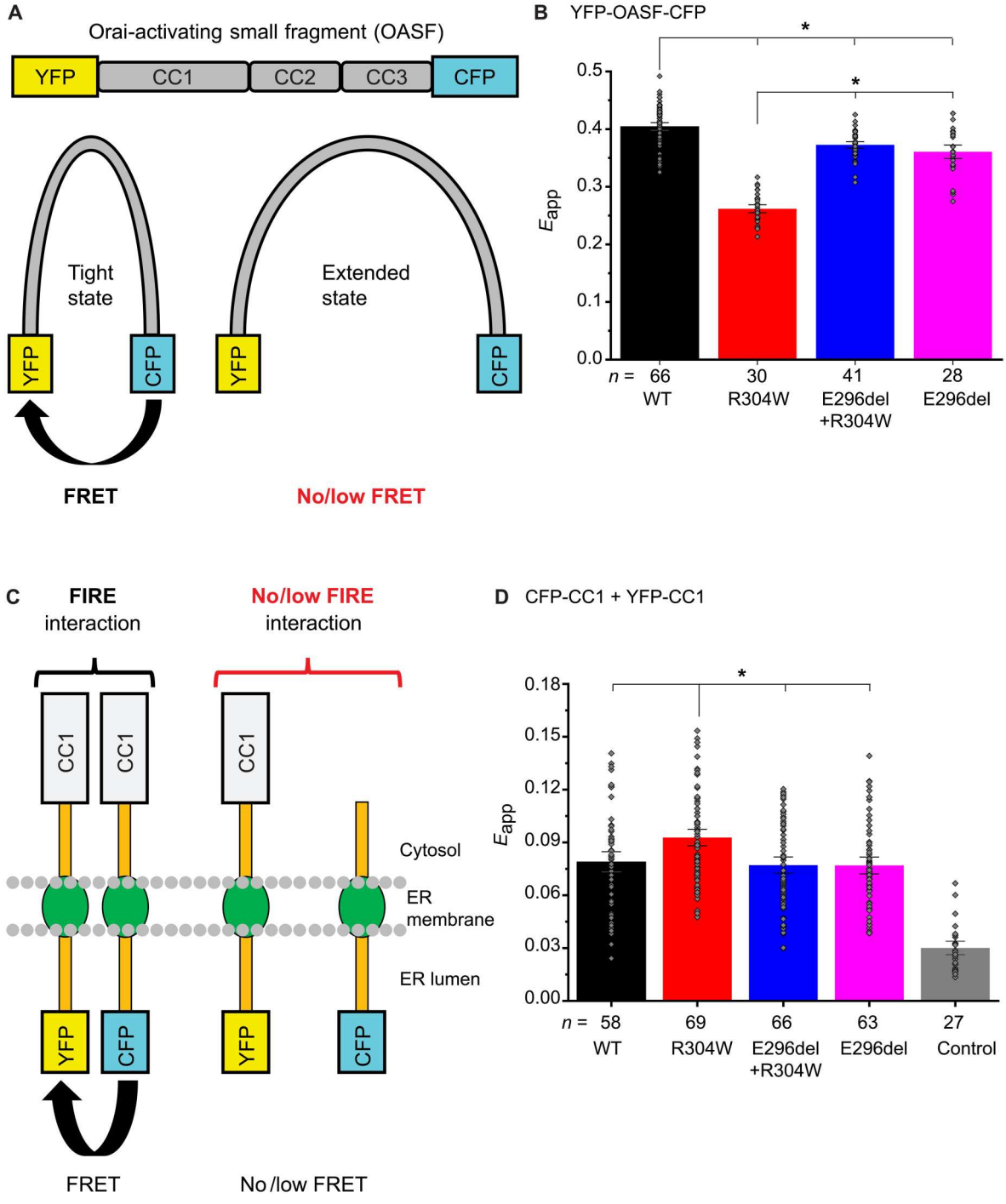

Fig. 3. FRET microscopy of OASF E296del+R304W and CC1 E296del+R304W. (**A**) The YFP-OASF-CFP conformational sensor, with the primary structure of OASF (top) and simplified representations of the tight and extended states of the protein fragment (bottom) depicted. In the tight state, the two fluorophores CFP and YFP (cyan and yellow rectangles) are in closer proximity to each other, which translates to higher FRET efficiency. (**B**) Intramolecular FRET transfer efficiency (E_{app}) showing conformational changes of YFP-OASF-CFP WT, R304W, E296del+R304W, and E296del when expressed in HEK293 cells. (**C**) Schematic representation of the FIRE system. Upon homomerization in the cytosol, the two fluorophores in the ER lumen (CFP and YFP) come into closer proximity to each other, leading to the occurrence of FRET. A control experiment using a construct that does not result in FIRE interaction is shown on the right. (**D**) Intermolecular FIRE homomerization of CFP-/YFP-CC1 WT, R304W, E296del+R304W, and E296del when expressed in HEK293 cells. As a control, a CFP construct lacking the CC1 domain was coexpressed with YFP-CC1. Color code: WT (black), R304W (red), E296del+R304W (blue), E296del (magenta), and control (gray). *$P < 0.05$ by Student's two-tailed t test. Experiments were replicated on at least two different days using independent transfections with the indicated number of cells (n). Data represent mean values ± SEM.

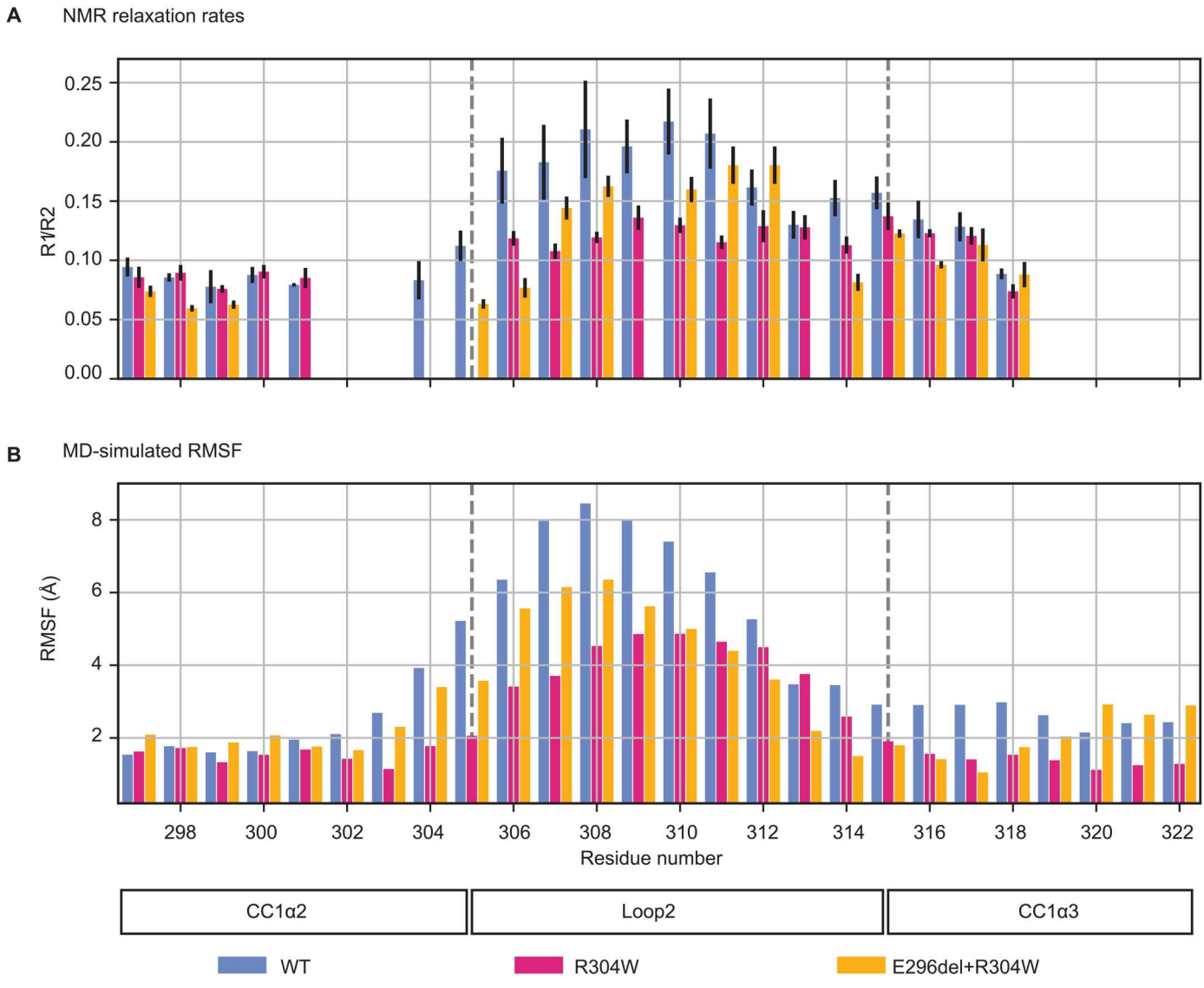

Fig. 4. Loop$_2$ flexibility measured in NMR relaxation studies and MD simulations of STIM1 CC1. (**A**) ^{15}N NMR relaxation studies with purified recombinant STIM1 CC1 fragments. A selection of assigned backbone amide resonances in and around the loop$_2$ region within CC1 WT, CC1 R304W, and CC1 E296del+R304W is shown. (**B**) Backbone root mean square fluctuation (RMSF) sampled during 1 μs of MD. Gray dashed lines indicate the starting and end points of loop$_2$ in the STIM1 CC1 NMR model. Note that for E296del+R304W, residue numbers of >296 were numbered as in the WT and R304W.

contact frequencies (or the time span during which contacts are formed as a fraction of the total MD simulation time) of residue 304 in the CC1 WT and mutant variants. We found that Trp^{304} formed relatively long-lived contacts with residues Met^{245}, Leu^{248}, Glu^{249}, and His^{252} located in CC1α1, with contact persistence close to 100%. By contrast, Arg^{304} in the WT and Trp^{304} in the double E296del+R304W mutant formed numerous, short-lived contacts, mostly with sequentially nearby polar residues such as Lys^{301}, Gln^{314}, or Tyr^{316} (Fig. 5, A and B). To test interactions between Trp^{304} and other residues within CC1α1 as suggested by the MD simulations, we developed an additional conformational FRET sensor construct: YFP-CC1α1-α2-CFP (Fig. 5C). As expected, YFP-CC1α1-α2-CFP WT yielded robust FRET efficiency (Fig. 5D). The R304W mutant had significantly higher FRET efficiency, in line with the MD simulation data, suggesting closer proximity due to a stronger interaction between residues of CC1α1 and Trp^{304} of CC1α2 (Fig. 5, A to D). The combination of E296del+R304W mutations significantly reduced FRET efficiency compared with the CC1α1-α2 R304W mutant, albeit to a higher level than for the WT FRET sensor. We additionally performed MD simulation–guided mutagenesis of residues Leu^{248} and Glu^{249}, which showed almost permanent contacts to Trp^{304} in MD simulations (Fig. 5, A and B). Introducing these two mutations, L248S+E249S, into the CC1α1-α2 R304W sensor attenuated the increase in intramolecular FRET caused by the R304W mutant to the level of the WT sensor (Fig. 5E). The YFP-CC1α1-α2-CFP conformational sensor data therefore revealed the persistence of contacts of R304W with residues within CC1α1, which was reduced in the E296del+R304W mutant (Fig. 5A). In summary, both MD simulations and FRET sensor measurements indicated that CC1α1-CC1α2

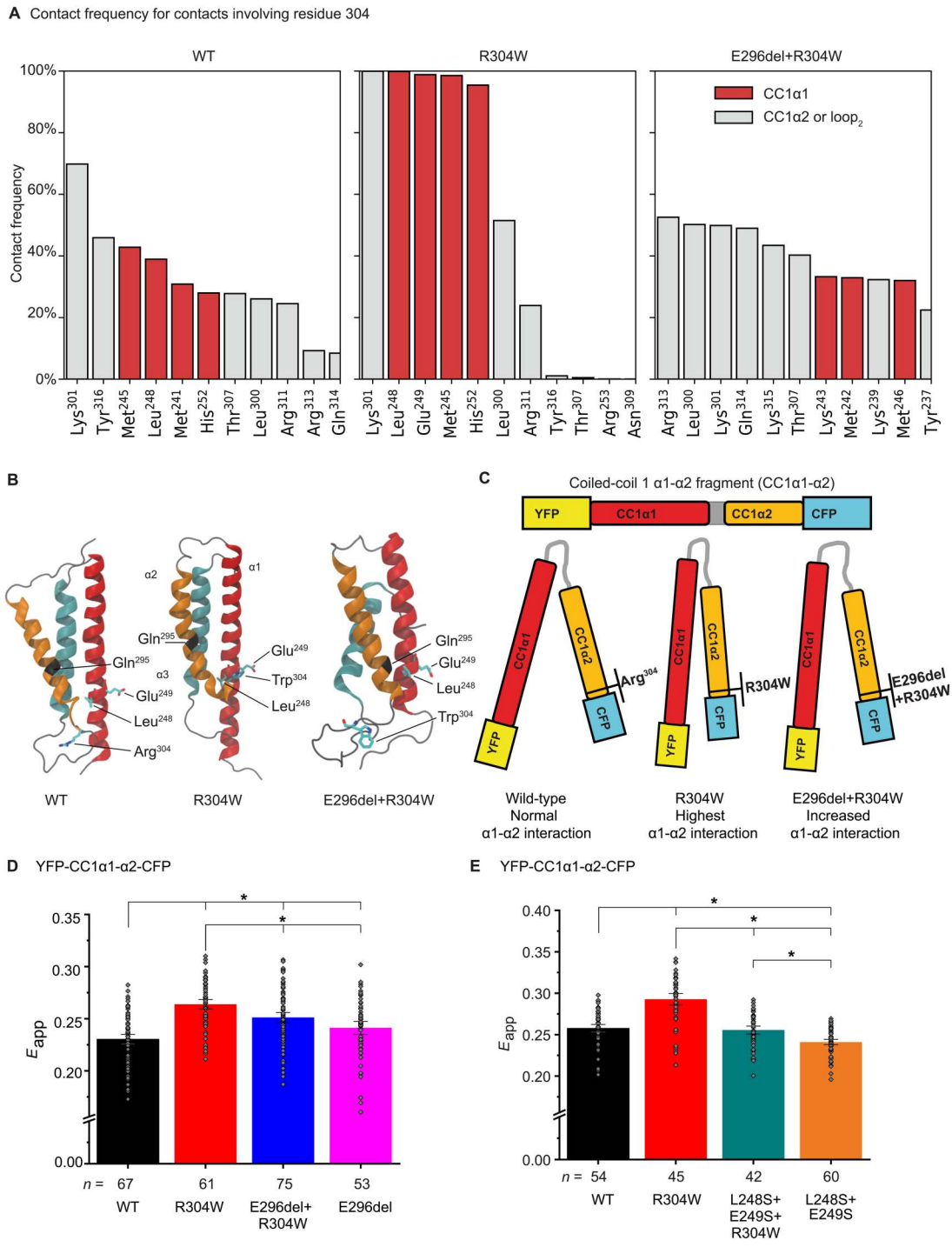

Fig. 5. Impact of E296del on the CC1α1-CC1α2 interaction. (**A**) Contact frequency for contacts involving Arg^{304} and Trp^{304}, respectively. Contacts between residue 304 and residues within CC1α1 are highlighted in red. Note that for E296del+R304W, residue numbers of >296 were numbered as in the WT and R304W. (**B**) In silico models of the R304W and E296del+R304W mutants. The helices CC1α1, CC1α2, and CC3 are colored in red, orange, and cyan, respectively. The residues Leu^{248}, Leu^{251}, and Trp^{304} are shown in licorice representation. Position 295 (the residue immediately upstream of the deletion) is marked by a black stripe. (**C**) The YFP-CC1α1-α2-CFP conformational sensor with the primary structure (top) and simplified representations of the effects of R304W or E296del+R304W on the conformation of the sensor (bottom) are depicted. In the STIM1 R304W construct, the two fluorophores CFP and YFP (cyan and yellow rectangles) are in closer proximity to each other, which translates to higher FRET efficiency. (**D**) Intramolecular FRET transfer efficiency (E_{app}) showing conformational changes in YFP-CC1α1-α2-CFP WT, R304W, E296del+R304W, and E296del when expressed in HEK293 cells. (**E**) Intramolecular FRET transfer efficiency (E_{app}) showing conformational changes in YFP-CC1α1-α2-CFP WT, R304W, L248S+E249S+R304W, and L248S+E249S when expressed in HEK293 cells. Color code: WT (black), R304W (red), E296del+R304W (blue), E296del (magenta), L248S+E249S+R304W (dark cyan), and L248S+E249S (orange). *$P < 0.05$ by Student's two-tailed t test. Conformational sensor experiments were replicated on at least two different days using independent transfections with the indicated number of cells (n). Conformational sensor data represent mean values ± SEM.

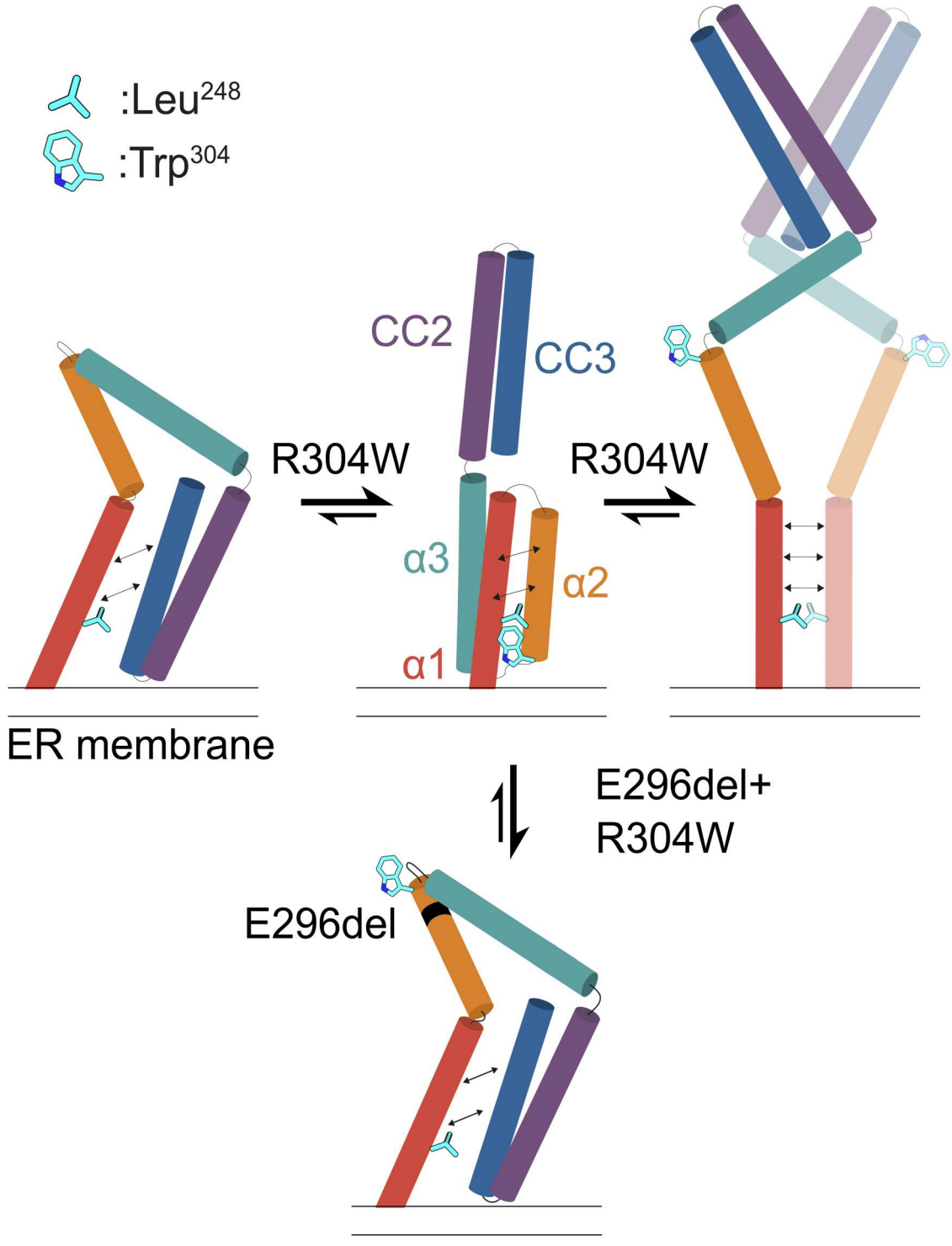

Fig. 6. Suggested competition between CC1α1-CC3 binding and CC1α1-CC1α2 binding in STIM1. The scheme illustrates the suggested competition between CC1α1-CC3 binding in the STIM1-inactive state (left) and CC1α1-CC1α2 binding promoted by R304W interacting with Leu^{248} (middle). E296del interferes with the CC1α1-CC1α2 interaction enforced by R304W and promotes a state with a conformation functionally and structurally almost equivalent to that of STIM1 WT (bottom). The conformation featuring the CC1α1-CC1α2 interaction (middle) is presumed to be one of several intermediate steps toward a fully elongated STIM1-active state (right). Trp^{304} and Leu^{248} are schematically drawn as individual residues. The deletion of Glu^{296} (E296del) is marked by a black stripe. CC1α1, CC1α2, and CC1α3 are shown in red, orange, and dark cyan, respectively. CC2 and CC3 (together representing CAD or SOAR) are shown in purple and blue, respectively. For simplicity, cytosolic STIM1 is depicted as OASF in the monomeric form in the left, middle, and bottom panels.

interactions were enhanced in the STIM1 R304W mutant and weakened when this mutation was combined with E296del (see Fig. 6). Hence, the R304W and E296del+R304W mutations affect STIM1 activation by altering interactions of CC1α1 with CC1α2 in opposing directions, with R304W promoting an extended state and E296del+R304W promoting a tight conformational state in full-length STIM1.

DISCUSSION

Here, we showed that the deletion of Glu^{296} in STIM1 antagonized the gain-of-function effect caused by the R304W mutation found in patients with Stormorken syndrome in vivo, in vitro, and in silico. Two independently generated mouse lines expressing STIM1 R304W both present with homozygous lethality, skeletal muscle degeneration, and abnormal bone architecture (*34*–*36*). In contrast, the double-mutant $Stim1^{E296del+R304W}$ mice presented here were phenotypically indistinguishable from WT mice, thus indicating that the deletion of Glu^{296} rescued the phenotype caused by STIM1 R304W. The rescue of the pathological phenotypes in mice was corroborated by the molecular characterization of STIM1 E296del+R304W by patch-clamp electrophysiology (Fig. 2A) and intermolecular and intramolecular FRET microscopy analyses (Figs. 2, B and C, and 3B). These data showed that STIM1 E296del+R304W phenotypically resembled STIM1 WT and that E296del conferred STIM1 R304W with the ability to retain a quiescent, tight state, enabling the double mutant to respond to changes in the ER Ca^{2+} store. HEK293 cells cotransfected with STIM1 E296del+R304W and Orai1 still showed a slight constitutive activation of Orai1 that was substantially higher than that in cells coexpressing STIM1 WT and Orai1 (Fig. 2A). As a result, the completely healthy phenotype of $Stim1^{E296del+R304W}$ mice is unexpected, especially with the residual constitutive Orai1 current activation observed in vitro. This difference between the in vitro and in vivo effects of STIM1 E296del+R304W may be due to the ectopic overexpression of the mutated protein in cells or may be because the slight constitutive activity is not sufficient to cause a measurable phenotypic effect in the $Stim1^{E296del+R304W}$ mice.

Molecular characterization of STIM1 E296del+R304W by NMR and MD simulations revealed that the Glu^{296} deletion partly restored flexibility of CC1 $loop_2$, facilitating the formation of the inhibitory CC1-CC3 clamp. Further, E296del returned the increased homomerization propensity of CC1 R304W back to WT levels. In addition, MD simulations revealed that the antagonizing effect of E296del on the STIM1 R304W mutation ensured weakening of the interaction between CC1α1 and CC1α2, in turn strengthening the CC1-CC3 clamp for stabilizing STIM1 in its quiescent, tight state (Fig. 6). Together, the experimental data in vivo and in vitro and MD simulations consistently corroborate the overall antagonizing effect of E296del on the R304W mutation.

We previously linked the activated state of STIM1 R304W to CC1α2 helix elongation and to increased CC1 homomerization (*6*). Here, we investigated the influence of E296del on helix elongation in the double mutant. The NMR relaxation ratios, which were consistent with the structure fluctuations in MD simulations, indicated that E296del partially restored the flexibility of the CC1α2-CC1α3 $loop_2$ in the double-mutant protein, likely by counteracting the R304W-induced elongation of the CC1α2 helix (Fig. 4, A and B). Accordingly, the propensity to form an elongated α-helical structure in the double mutant was intermediate between that for the WT protein and for the R304W mutant. The FIRE data complemented the NMR results by showing that E296del fully reduced the elevated CC1 R304W homomerization to WT levels. In addition, the intramolecular FRET studies with OASF also revealed a tight conformation, suggesting that the E296del+R304W double mutant had CC1-CC3 clamp interaction that was absent in the R304W mutant (Fig. 3B). Nonetheless, FRET efficiencies of both OASF E296del and E296del+R304W mutants were still substantially lower than that of OASF WT. At least in the soluble OASF fragment, E296del may have exerted a conformational effect on its own (Fig. 3B) that had functionally inconsequential effects on full-length STIM1 (Fig. 2, A to C).

In the in silico mutated R304W model, Trp^{304} clung to a hydrophobic site of CC1α1 (Fig. 5B). In particular, Trp^{304} formed tight contacts with Leu^{248} (Fig. 6), a residue that is crucially involved in the CC1α1 clamp interaction with the SOAR domain and thus in the fine-tuning of STIM1 activation (*11*). In the STIM1 E296del+R304W mutant, Trp^{304} cannot interact with Leu^{248} due to the helical wheel phase shift by the deletion (Fig. 5B). This suggested an additional effect by the deletion because it partially restored the quiescent state by reenforcing CC1α1-CC3 domain interactions, perhaps through the better accessibility of Leu^{248} (*11*, *41*). Our YFP-CC1α1-α2-CFP WT FRET sensor data supported this notion because mutation of Leu^{248} and Glu^{249} to serine residues in the R304W mutant (L248S+E249S+R304W) fully reduced the increase in intramolecular FRET caused by the R304W mutant to the level of the WT (Fig. 5E), suggesting a looser association between the CC1α1 and CC1α2 helices. This would be expected to favor a tighter CC1α1-CC3 interaction and a quiescent, tight state of the STIM1 E296del+R304W mutant (Fig. 6, bottom). Further, the helical wheel phase shift elicited by E296del is crucial for countering the functional effects of the R304W mutation in STIM1 R304W and OASF R304W, whereupon a shift in either direction can disrupt the proposed interaction between Trp^{304} and Leu^{248}. This is showcased by several other deletions (Q295del, A297del, and Q298del) and the insertion of an additional alanine between Glu^{296} and Ala^{297} (E296_A297insA), all of which behaved similarly to E296del when combined with R304W. However, deletions within $loop_2$ (G306del and T307del) downstream of R304W did not elicit effects comparable to those of E296del because Trp^{304} is upstream of these deletions and is not affected by a helical wheel phase shift (fig. S3, A to F). The delicate balance of interactions between coiled-coil domains (*13*) makes them a promising target of pharmacological interference (*42*) for control of the activation state of STIM1.

In conclusion, we provide evidence that the pathogenic effects of the STIM1 R304W mutation, which is the most frequently observed mutation in patients with Stormorken syndrome, are antagonized through the in cis deletion of Glu^{296}. This deletion allows the STIM1 protein structure to change from a constitutively extended, active state to a state similar, but not identical, to that of the WT protein that is nonetheless sufficient to reverse the pathological STIM1 R304W phenotypes in mice.

MATERIALS AND METHODS

Establishment of mouse line expressing STIM1 E296del+R304W

We previously established a mouse line expressing *Stim1* (NC_000073.6): g.102421471A>T;p.R304W (GRCm38.p6/mm10) (Stim1^{R304W}) using the CompoZr Zinc Finger technology (Sigma-Aldrich, Missouri, USA) on F1 (C57BL/6J × CBA) background (*34*). In parallel, a double-mutant mouse line carrying a 3-bp deletion: *Stim1* (NC_000073.6): g.102421448-102421450delAAG;p.E296del (GRCm38.p6/mm10), in cis with the R304W mutation, was likely generated as a by-product of an error-prone nonhomologous end-joining repair mechanism. For simplicity, we apply the WT residue numbering for the double mutant as well (meaning that throughout the paper, Trp^{304} refers to the 303rd residue in the double mutant). The line was named Stim1$^{E296del+R304W}$. Identification of the Stim1$^{E296del+R304W}$ founder mouse was verified by Sanger sequencing as previously described (*34*). Whole-genome sequencing of the female founder mouse DNA was performed commercially and was analyzed as previously described (Novogene, Beijing, China) (*34*). A total of 740,316,082 reads were obtained with a 99.29% mapping rate. The whole-genome coverage was 90.8% at 1×, 89.8% at 5×, and 87.1% at 15× read depth. Mean read depth was 27.6×, and the median read depth was 30×. The founder female was then backcrossed to a C57bl/6J male mouse (Harlan laboratories, Indianapolis, USA) and further intercrossed to establish the Stim1$^{E296del+R304W}$ colony.

Maintenance of mice

Animals were housed under standard conditions (12-hour light/12-hour dark cycle, 21° ± 2°C temperature, and 55 ± 5% relative humidity) with ad libitum access to water and standard chow. Growth of mice was monitored weekly through body weight measurements. Animal experimental protocols for generation, breeding, and use of transgenic animals were registered and approved by the Norwegian Food Safety Authority [Mattilsynet, Experimental animal welfare supervision and application system (FOTS) ID 7216, 5873, and 14205] and followed the ethical guidelines given in Directive 2010/63/EU of the European Parliament on the protection of animals used for scientific purposes.

Necropsy

Full necropsies and histological examinations of eight heterozygous Stim1$^{E296del+R304W}$ and eight homozygous Stim1$^{E296del+R304W}$ mice were performed as previously described when mice were euthanized at 5 to 6 months of age (*34*). H&E staining of formalin-fixed tissue sections was performed in parallel to samples from Stim1^{R304W} and WT mice, and the sections were evaluated for the severity of the phenotype in each genotype in a blinded fashion.

Exercise endurance testing on treadmill

Exercise endurance of homozygous and heterozygous Stim1$^{E296del+R304W}$ mice (10 female and 10 male mice per genotype; n = 20 mice in total per genotype) were measured as described previously in a five-lane mouse treadmill equipped with an electric grid (Panlab-Harvard apparatus, Barcelona, Spain) (*34*). In brief, the mice were run on the treadmill until exhaustion after a 2-day acclimatization to the instrument with a mild electric shock of 0.2 A (adjustable from 0 to 2) activated at 5-s intervals. Exhaustion was defined as inability to continue running after mild electric shock, standing on electric grid for >4 s, or running close to the grid for >5 s. The time and distance run before reaching exhaustion were recorded. All Stim1$^{E296del+R304W}$ mice were run in parallel to age-matched WT and Stim1^{R304W} mice. To reduce bias, the experiment run and scoring of parameters were done in the absence of genotype information.

Flow cytometry studies on platelets

STIM1 expression in platelets was measured in WT, heterozygous Stim1^{R304W}, and homozygous Stim1$^{E296del+R304W}$ mice as previously described (*34*). In brief, whole blood samples were fixed in 4% paraformaldehyde, followed by red blood cell lysis using red blood cell lysis buffer. Platelet/white blood cells (WBC) was pelleted and washed, and cell counts were normalized. The cells were permeabilized with 0.5% Triton X-100 (Sigma-Aldrich), pelleted, resuspended with phosphate-buffered saline (PBS) + 1% bovine serum albumin, and costained with STIM1 antibody (final concentration of 5 μg/ml) and the platelet marker glycoprotein IX–Alexa Fluor 647. To detect the STIM1 antibody, we used Alexa Fluor 488–α-rabbit as secondary antibody at a 1:1000 dilution. Cells were pelleted, resuspended in 1× PBS, and analyzed by flow cytometry.

μCT analysis of the tibia

Morphological indices of metaphyseal regions of tibia were measured using μCT scanning as previously described (*35*). In brief, bone samples were formalin-fixed, wrapped in plastic foil, rotated longitudinally at 0.4°, and imaged with pixel size = 5 μm; peak tube potential = 100 kV; x-ray intensity = 100 μA; and 0.5-mm aluminum filter using Bruker Skyscan 1172 (Bruker, Kontich, Belgium). Raw images were reconstructed to three-dimensional cross-sectional image data sets using a three-dimensional cone beam algorithm on NRecon Reconstruction Software (Microphotonics Inc., Allentown, PA). On the basis of thickness and structural differences, cortical and trabecular bone were separated in CT-Analyzer with a custom processing algorithm, and cortical bone parameters (mean total cross-sectional area, cortical bone volume, and cortical bone area), and trabecular bone parameters (trabecular separation, trabecular bone volume fraction, and trabecular number) were analyzed as comparison of means with Student's t test.

Statistics

The number of mice was calculated adhering to the 3R principle, and the estimate was made on the basis of requirements for statistical significance, with the expectation of eight mice per litter and the consideration of the lowest possible number of mice required to obtain statistically relevant results. Results for the mouse model are presented as means ± SEM. Statistical analyses and relative graphical representation were performed using the Student's t test together with the F test for variances and the Shapiro-Wilk test for normal distribution or the Mann-Whitney U test (as specified in figures) in GraphPad Prism 7 (GraphPad Software Inc., CA, USA). For the in vitro model, OriginPro 2020 (OriginLab Corporation, MA, USA) was used for all statistical analyses and graph plots. Results are depicted as mean values ± SEM (NMR: mean values ± SD) determined from the indicated number (n) of repeats from at least two independent experiments. The Student's two-tailed t test together with the F test of equality of variances was used for statistical analyses, with

differences considered statistically significant at $P < 0.05$. The one-sample Kolmogorov-Smirnov test was used to verify the presence of a normal distribution for the analyzed datasets. The Grubbs test was applied to eliminate outliers.

Molecular cloning and mutagenesis

Human Orai1 (accession number NM_032790) was generously supplied by A. Rao (Harvard Medical School). N-terminally tagged Orai1 was engineered using Sal I and Sma I restriction sites of the pEYFP-C1 vector (Clontech Laboratories, CA, USA). C-terminally tagged Orai1 was cloned using the Xho I and Bam HI sites of the pEYFP-N1 vector. For unlabeled Orai1, the Orai1 coding region was cloned by polymerase chain reaction into the T/A site of pCDNA3.1V5-His TOPO expression vector. N-terminally pECFP- and pEYFP-labeled human STIM1 (accession number NM_ 003156) were from T. Meyer (Stanford University). C-terminally pECFP-tagged STIM1 was purchased from GeneCopoeia (catalog number EX-S0521-M02). N-terminal pECFP-STIM1 mutants (R304W, E296del, E296del+R304W, Q295del, Q295del+R304W, A297del, A297del+R304W, L251S, L251S+E296del, L416S+L423S, E296del+L416S+L423S, Q298del+R304W, G306del+R304W, T307del+R304W, and E296_A297insA+R304W), N-terminal pEYFP-STIM1 mutants (R304W, E296del, and E296del+R304W), and C-terminal pECFP-STIM1 mutants (R304W, E296del, and E296del+R304W) were generated with a QuikChange XL site-directed mutagenesis kit (Stratagene, CA, USA). To generate double-tagged STIM1-OASF constructs, we introduced CFP into pEYFP-C2 with Sac II and Xba I, and the OASF fragment (amino acids 233 to 474) of STIM1 was inserted using restriction sites Eco RI and Sac II. Double-tagged YFP-OASF-CFP mutants (R304W, E296del, E296del+R304W, Q295del, Q295del+R304W, A297del, A297del+R304W, L251S, L251S+E296del, L416S+L423S, E296del+L416S+L423S, Q298del+R304W, G306del+R304W, T307del+R304W, and E296_A297insA+R304W) were generated with the QuikChange XL site-directed mutagenesis kit (Stratagene). YFP-CC1α1-α2-CFP was engineered by exchanging OASF with the CC1α1-α2 fragment 233 to 309. Point mutations (R304W, E296del, E296del+R304W, L248S+E249S, and L248S+E249S+R304W) were generated with the QuikChange XL site-directed mutagenesis kit (Stratagene). Constructs used for the FIRE system (C-TMG and Y-TMG) contained the STIM1-signal peptide followed by ECFP (C) or EYFP (Y), a 29–amino acid linker, the STIM1 TM domain (TM), and a flexible linker consisting of 32 glycine (G) residues followed by the protein fragment of interest (CC1; amino acids 233 to 343). The QuikChange XL site-directed mutagenesis kit (Stratagene) was used to generate C- and Y-TMG point mutants (R304W, E296del, and E296del+R304W). For NMR experiments, STIM1 CC1 (amino acids 233 to 343) was cloned into the pGEX4T1 vector. Point mutants (R304W and E296del+R304W) were produced with the QuikChange XL site-directed mutagenesis kit (Stratagene). The sequences of all primers that were used are listed in table S1. Constructs were verified by sequence analysis.

Patch-clamp electrophysiology

Patch-clamp electrophysiology recordings of HEK293 cells (DSMZ–German Collection of Microorganisms and Cell Cultures GmbH) were carried out at room temperature 24 to 36 hours after transfection. The whole-cell configuration was exclusively used in all experiments, with two Ag/AgCl electrodes serving as both recording and reference electrodes. A 1-s voltage ramp covering the range of −90 to +90 mV was applied every 5 s; the holding potential was thereby set to 0 mV. The current amplitudes recorded at −74 mV during every voltage ramp were used for data evaluation. The intracellular pipette solution was used for passive store depletion and consisted of 145 mM Cs methane sulfonate, 20 mM EGTA, 10 mM Hepes, 8 mM NaCl, and 5 mM $MgCl_2$ (pH 7.2). The standard extracellular solution contained 145 mM NaCl, 10 mM Hepes, 10 mM $CaCl_2$, 10 mM glucose, 5 mM CsCl, and 1 mM $MgCl_2$ (pH 7.4). The junction potential of −12 mV that was caused by the use of a sulfonate-based pipette solution and a Cl^--based extracellular solution was not considered, and leak correction was applied to all recordings. For store-dependent currents, the initial current amplitude recorded during the voltage ramp applied immediately after the whole-cell configuration was subtracted from all subsequent current amplitudes. For constitutively active currents, a current amplitude obtained during a voltage ramp applied after perfusion with 10 μM La^{3+} at the end of the experiment was used instead. Last, individual experiments were normalized to compensate for potential cell dimension-related effects by dividing all current amplitudes by the whole-cell capacitance, resulting in current density in picoampere per picoFarad (pA/pF) as unit of measurement. The WinWCP software package (v4.2.2, University of Strathclyde, UK) was used for data recording and processing.

FRET microscopy

Confocal FRET microscopy of HEK293 cells (DSMZ–German Collection of Microorganisms and Cell Cultures GmbH) was carried out at room temperature 24 to 36 hours after transfection. For the experimental setup, the CSU-X1 Real-Time Confocal System (Yokogawa Electric Corporation, Japan) fitted with two CoolSNAP HQ2 charge-coupled device cameras (Photometrics, AZ, USA) was used. In addition, a dual-port adapter (dichroic: 505lp, cyan emission filter: 470/24, yellow emission filter: 535/30; Chroma Technology Corporation, VT, USA) was part of the installation. This configuration was connected to an Axio Observer.Z1 inverted microscope (Carl Zeiss, Oberkochen, Germany) with two diode lasers (445 and 515 nm; Visitron Systems, Puchheim, Germany). All components were placed on a Vision IsoStation antivibration table (Newport Corporation, CA, USA). The VisiView software package (v2.1.4, Visitron Systems) was used for controlling the confocal system and image recording. Because of cross-excitation and spectral bleed-through, it was necessary to perform image correction before any kind of FRET calculation. Therefore, cross-excitation calibration factors were experimentally determined for all expressed DNA constructs on each day that measurements were performed. Threshold determination and background signal subtraction were applied to calculate the apparent FRET efficiency E_{app}. This was done on a pixel-to-pixel basis using a custom program (*43*) integrated into MATLAB (v7.11.0, the MathWorks Inc., MA, USA) and implementing a previously described method (*44*) with a microscope-specific constant G parameter of 2.75.

Nuclear magnetic resonance

The STIM1 CC1 fragments (WT, R304W, and E296del+R304W) were prepared as described previously (*32*). NMR experiments were recorded using a 700-MHz Avance III spectrometer (Bruker Corporation, MA, USA; equipped with a Bruker TCI cryoprobe,

with radiofrequency coils cooled to 20 K and $^{1}H,^{13}C,^{2}H$ preamplifiers at 77 K) at the Austro-Czech RERI-uasb NMR center located at Johannes Kepler University Linz. The basic set of recorded double- and triple-resonance assignment experiments is described in (*6*). Additional carbon-detected NMR assignment experiments (CON, CACO, CBCACO, CBCACON, and CANCO) were recorded at CERM Institute in Sesto Fiorentino using a 700-MHz Bruker Avance spectrometer equipped with a cryogenically cooled carbon-detection Bruker TCO probe. The samples were measured in various types of NMR tubes: 5-mm round tubes (Wilmad LabGlass, NJ, USA) with a working volume of 550 to 600 µl, 5-mm shaped tubes (Bruker Corporation) with a working volume of 330 µl, and 5-mm Shigemi tubes (Bruker Corporation) with a working volume of 230 µl. Measurements were recorded at a sample temperature of 310 K using the TopSpin software package (v3.5, Bruker Corporation). ^{15}N-T_1 and ^{15}N-T_2 relaxation times for CC1 WT and R304W were derived from exponential fitting of peak heights in sets of ^{15}N-HSQC experiments with different relaxation delays. T_1 relaxation delays: 20, 40, 80, 160, 250, 320, 500, 640, 800, 1200, 1500, and 2000 ms; T_2 relaxations delays: 8.48, 16.96, 25.44, 33.92, 42.40, 50.88, 67.84, 84.80, 101.76, 118.72, 135.68, 169.60, 203.52, 220.48, and 237.44 ms. For the E296del+R304W mutant, the T_2 delays were set to 20, 30, 40, 45, 50, 55, 60, 70, 80, 90, 100, 110,130, 150, 170, 190, and 200 ms. The resonance assignment data for WT, R304W, and E296del+R304W were deposited in the Biological Magnetic Resonance Data Bank (BMRB) under entry IDs 50114, 50118, and 51173, respectively.

MD simulation preparations

Protein electrostatic calculations (*45*) were used to assign protonation states to titratable residues. Electrostatic potentials for the protein in a dielectric medium were computed with TAPBS (*46*). Atomic coordinates were taken from the NMR CC1 model (*13*) (Protein Data Bank ID 6YEL), a dielectric constant $\varepsilon = 80$ was used for the surrounding aqueous environment, and $\varepsilon = 4$ was assigned to the protein interior. For the ion-inaccessible region around the protein, an ion radius of 2 Å was used. The protein volume was determined by rolling a spherical water probe with a radius of 1.4 Å over the molecule, using a grid with 3 points/Å^2 (*47*). Protonation patterns were sampled using KARLSBERG 2.0 (*48*). We then assigned those protonation states that occur with highest probability at pH = 7. Glutamic acid residues 255, 296, and 310 were set to their protonated states. Histidine residues 338, 252, and 259 were set to their deprotonated states with a hydrogen placed on the delta nitrogen. His^{266} and His^{281} were deprotonated with a hydrogen on the epsilon nitrogen. His^{240} and His^{272} were protonated: They carried both a delta and an epsilon hydrogen. All other titratable residues were set to their standard protonation states. The same protonation states were used for the R304W and E296del+R304W models.

The protein was solvated in a TIP3P water box with dimensions of 92 Å by 91 Å by 91 Å using the CHARMM-GUI input generator (*49*, *50*). The water box was neutralized by adding one potassium ion. The WT system contained the 115–amino acid CC1 structure, 1 potassium ion, and 22,373 water molecules.

Modeling mutant molecules

To model the R304W mutant, we used the NMR CC1 WT structure (*13*) and introduced the point mutation R304W using CHARMM. Because E296del+R304W exhibits store-dependent function and thus resembles WT, we again based our model on the CC1 WT structure. To manipulate CC1α2 separately, we first unfolded the WT structure using a bias potential that raised the root mean square deviation (RMSD) and the radius of gyration while keeping helical secondary structure elements intact. Glu^{296} in CC1α2 was then manually deleted. The two resulting fragments of CC1α2 were reassembled using CHIMERA (*51*), and the R304W mutation was applied using CHARMM. CC1α2 was restored into a perfect α helix with a harmonic restraint applied to the Nanoscale Molecular Dynamics (NAMD) collective variable (CV) alpha. The structure was then bent into a three-helix bundle using targeted MD (*52*), in which backbone atoms in CC1α1 to CC1α3 targeted the corresponding positions in the NMR WT model. CC1α2 was again optimized with a harmonic potential. The folded structure was embedded in a water box (88 Å by 78 Å by 79 Å) and equilibrated during 60 ns of restrained MD while restraining the backbone RMSD with respect to the WT structure to values below 3.5 Å. This was followed by 160 ns of unrestrained MD. The first five N-terminal residues, which are not part of the native sequence (*13*), were deleted. The resulting structure was embedded and equilibrated in a new neutralized water box with dimensions of 102 Å by 74 Å by 70 Å containing 15,872 water molecules and one sodium ion. The E296del+R304W model was equilibrated over 120 ns. To suppress tumbling motion of the protein, we restrained the positions of CC1α1 backbone atoms, allowing us to use an elongated water box of 102 Å by 74 Å by 70 Å and thereby save computation time. To model the WT with a deprotonated R304, we used the partial charges provided by the software TAPBS and created a corresponding entry in our CHARMM residue topology file. The adapted partial charges were then patched into the NMR model structure. After equilibration, the deprotonated model was simulated for 700 ns.

Simulation protocol for conventional MD

MD simulations were performed using NAMD 2.13 (*53*) and the CHARMM36m force field (*54*). We first minimized our structure and heated it from 100 to 300 K over the course of 200 ps. CA positions were fixed with a restraint potential. This backbone restraint was gradually released over the course of 1 ns. We ran 1 µs of unrestrained production simulations for the WT and the R304W and E296del+R304W mutants, respectively. We used the *NpT* ensemble with a constant temperature of 300 K using Langevin dynamics. The pressure was set to 1 atm with the Langevin piston method. The particle-mesh Ewald method was used for long-range electrostatic interactions. MD was calculated using the velocity Verlet algorithm with an integration time step of 2 fs. H-bonds were restrained using ShakeH.

Trajectory analysis

We applied the WT residue numbering to the deletion mutant, such that Trp^{304} refers to the 303rd residue, but for consistency, residue numbers >296 are shifted such that said residue was still named Trp^{304}. Trajectories were analyzed using the pytraj (*55*, *56*) and MDTraj (*57*) packages. Contact persistence was calculated with the contact map explorer plugin for MDTraj using a cutoff distance of 4.5 Å. Secondary structure maps were created using the Define Secondary Structure of Proteins (DSSP) algorithm as implemented in MDTraj. Interhelical interaction energies were calculated using

CHARMM. Nonbonded interaction pairs were created with a cutoff of 14 Å. Interactions were calculated with a distance cutoff of 12 Å and a switching distance of 10 Å. Interaction energies for interactions between residue 304 and its neighbors were calculated using gRINN (*58*). Interaction energies were calculated for pairs of residues with distances below 20 Å in at least 60% of all trajectory frames. Energies were calculated with a distance cutoff of 12 Å.

Dihedral metadynamics

We used well-tempered metadynamics (*59*) for our dihedral FES calculations. We specified the dihedral angles ϕ and ψ of residue 304 as our CVs. The initial Gaussian height was set to 0.1 kcal/mol, and the bias temperature was set to 1500 K. New Gaussians were added every 2 ps. Hill width was set to 15°. Simulations were propagated for 150 ns for the WT and the R304W mutant, respectively. Convergence was checked by monitoring the free energy difference between selected minima. The mean error as calculated with block averaging converged to about 1.4 kcal/mol with increasing block size (*60*).

Helicity metadynamics

To calculate the free energy of helical content in $loop_2$ using well-tempered metadynamics, we chose a hydrogen bond helicity score h and the helical $RMSD_\alpha$ as our CVs. The hydrogen bond score h measures the formation of hydrogen bonds between atoms $O^{(n)}$ and $N^{(n+4)}$ for residues N_0 to $N_0 + N$ by monitoring whether the positions $\mathbf{x}_{O^{(n)}}$ and $\mathbf{x}_{N^{(n+4)}}$ are closer than a cutoff distance d_0. Together

$$h\left(\left\{O^{(n)},\ N^{(n+4)}\right\}_{n=N_0,\ldots,N_0+N-4}\right) = \frac{1}{N-4}\sum_{n=N_0}^{N_0+N-4}\frac{1-\left(\left|\mathbf{x}_{O^{(n)}}-\mathbf{x}_{N^{(n+4)}}\right|/d_0\right)^n}{1-\left(\left|\mathbf{x}_{O^{(n)}}-\mathbf{x}_{N^{(n+4)}}\right|/d_0\right)^m}$$

Choosing $d_0 = 3.3$ Å, $n = 6$, and $m = 9$, a value $h = 1$ corresponds to fully formed hydrogen bonds between all O and N atoms under consideration. $h = 0$ suggests the absence of such bonds. To calculate h, we used the CV alpha from the NAMD colvars module (*61*) and set the parameter hBondCoeff to 1. Our second CV measures the RMSD with respect to a fully formed helix. As a reference for the complete helix, we used either structures taken from preliminary metadynamics runs or structures taken from short MD simulations that maximized $loop_2$ helical content with a restraint potential. The two CVs were applied to residues 310 to 317. For the E296del+R304W mutant, residue numbering is shifted such that the metadynamics bias is applied to the same sequence of residues.

Well-tempered metadynamics simulations were carried out with a hill weight of 0.1 kcal/mol and a hill width of 0.01 units (for h) and 0.2 Å (for $RMSD_\alpha$), respectively. The bias temperature was set to 10,000 K. New Gaussian hills were added each picosecond. Because the quality of our CVs decreases in the low-helicity regime, the range $h < 0.12$ was barred off. To test our CVs and ensure reproducibility, we performed several independent well-tempered metadynamics runs. Although the individual simulations did not perfectly agree, we observed differences in the free energy surfaces obtained for the different protein types. For the WT and the R304W and E296del+R304W mutants, we ran four, four, and five metadynamics runs, respectively, each with a run length of 300 ns. Convergence was again checked by monitoring the free energy difference between selected minima. We monitored the CV trajectories for signs of hysteresis but found none. For each frame, $loop_2$ residues were assigned a secondary structure with the DSSP algorithm. To track secondary structure over time, we set up an array (the "secondary structure trajectory") in which 1s represent helical conformations and 0s represent nonhelical conformations. To obtain the probability of helical conformation in the unbiased ensemble for each residue, we reweighted the secondary structure trajectory with an algorithm described previously (*62*). Given these weights, the residue-wise probability of helical conformation is given by the weighted average over each secondary structure trajectory. In calculating the weighted average, we concatenated secondary structure trajectories and (normalized) weights obtained from individual runs and treated them as one pooled ensemble. As an additional validation of the metadynamics convergence, this procedure allowed us to compare free-energy profiles calculated from the deposited metadynamics Gaussians and the reweighted CV trajectories, which were satisfactorily similar for all runs.

Supplementary Materials

This PDF file includes:
Figs. S1 to S9
Table S1

Other Supplementary Material for this manuscript includes the following:
MDAR Reproducibility Checklist

View/request a protocol for this paper from *Bio-protocol*.

REFERENCES AND NOTES

1. R. M. Luik, B. Wang, M. Prakriya, M. M. Wu, R. S. Lewis, Oligomerization of STIM1 couples ER calcium depletion to CRAC channel activation. *Nature* **454**, 538–542 (2008).
2. J. W. Putney Jr., Capacitative calcium entry: Sensing the calcium stores. *J. Cell Biol.* **169**, 381–382 (2005).
3. J. Liou, M. L. Kim, W. do Heo, J. T. Jones, J. W. Myers, J. E. Ferrell Jr., T. Meyer, STIM is a Ca^{2+} sensor essential for Ca^{2+}–store-depletion-triggered Ca^{2+} influx. *Curr. Biol.* **15**, 1235–1241 (2005).
4. S. L. Zhang, Y. Yu, J. Roos, J. A. Kozak, T. J. Deerinck, M. H. Ellisman, K. A. Stauderman, M. D. Cahalan, STIM1 is a Ca^{2+} sensor that activates CRAC channels and migrates from the Ca^{2+} store to the plasma membrane. *Nature* **437**, 902–905 (2005).
5. M. Fahrner, M. Muik, R. Schindl, C. Butorac, P. Stathopulos, L. Zheng, I. Jardin, M. Ikura, C. Romanin, A coiled-coil clamp controls both conformation and clustering of stromal interaction molecule 1 (STIM1). *J. Biol. Chem.* **289**, 33231–33244 (2014).
6. M. Fahrner, M. Stadlbauer, M. Muik, P. Rathner, P. Stathopulos, M. Ikura, N. Müller, C. Romanin, A dual mechanism promotes switching of the Stormorken STIM1 R304W mutant into the activated state. *Nat. Commun.* **9**, 825 (2018).
7. S. O. Sage, Three routes for receptor-mediated Ca^{2+} entry. *Curr. Biol.* **2**, 312–314 (1992).
8. M. M. Wu, R. M. Luik, R. S. Lewis, Some assembly required: Constructing the elementary units of store-operated Ca^{2+} entry. *Cell Calcium* **42**, 163–172 (2007).
9. I. Derler, I. Jardin, C. Romanin, Molecular mechanisms of STIM/Orai communication. *Am. J. Physiol. Cell Physiol.* **310**, C643–C662 (2016).
10. B. A. McNally, A. Somasundaram, A. Jairaman, M. Yamashita, M. Prakriya, The C- and N-terminal STIM1 binding sites on Orai1 are required for both trapping and gating CRAC channels. *J. Physiol.* **591**, 2833–2850 (2013).
11. M. Muik, M. Fahrner, R. Schindl, P. Stathopulos, I. Frischauf, I. Derler, P. Plenk, B. Lackner, K. Groschner, M. Ikura, C. Romanin, STIM1 couples to ORAI1 via an intramolecular transition into an extended conformation. *EMBO J.* **30**, 1678–1689 (2011).
12. M. Fahrner, H. Grabmayr, C. Romanin, Mechanism of STIM activation. *Curr. Opin. Physiol.* **17**, 74–79 (2020).

13. P. Rathner, M. Fahrner, L. Cerofolini, H. Grabmayr, F. Horvath, H. Krobath, A. Gupta, E. Ravera, M. Fragai, M. Bechmann, T. Renger, C. Luchinat, C. Romanin, N. Müller, Interhelical interactions within the STIM1 CC1 domain modulate CRAC channel activation. *Nat. Chem. Biol.* **17**, 196–204 (2021).
14. N. Hirve, V. Rajanikanth, P. G. Hogan, A. Gudlur, Coiled-coil formation conveys a STIM1 signal from ER lumen to cytoplasm. *Cell Rep.* **22**, 72–83 (2018).
15. C. Y. Park, P. J. Hoover, F. M. Mullins, P. Bachhawat, E. D. Covington, S. Raunser, T. Walz, K. C. Garcia, R. E. Dolmetsch, R. S. Lewis, STIM1 clusters and activates CRAC channels via direct binding of a cytosolic domain to Orai1. *Cell* **136**, 876–890 (2009).
16. J. P. Yuan, W. Zeng, M. R. Dorwart, Y. J. Choi, P. F. Worley, S. Muallem, SOAR and the polybasic STIM1 domains gate and regulate Orai channels. *Nat. Cell Biol.* **11**, 337–343 (2009).
17. D. E. Clapham, Calcium signaling. *Cell* **131**, 1047–1058 (2007).
18. M. Prakriya, S. Feske, Y. Gwack, S. Srikanth, A. Rao, P. G. Hogan, Orai1 is an essential pore subunit of the CRAC channel. *Nature* **443**, 230–233 (2006).
19. M. J. Berridge, Calcium signalling remodelling and disease. *Biochem. Soc. Trans.* **40**, 297–309 (2012).
20. S. Feske, CRAC channelopathies. *Pflugers Arch.* **460**, 417–435 (2010).
21. R. S. Lacruz, S. Feske, Diseases caused by mutations in ORAI1 and STIM1. *Ann. N. Y. Acad. Sci.* **1356**, 45–79 (2015).
22. M. Byun, A. Abhyankar, V. Lelarge, S. Plancoulaine, A. Palanduz, L. Telhan, B. Boisson, C. Picard, S. Dewell, C. Zhao, E. Jouanguy, S. Feske, L. Abel, J. L. Casanova, Whole-exome sequencing-based discovery of STIM1 deficiency in a child with fatal classic Kaposi sarcoma. *J. Exp. Med.* **207**, 2307–2312 (2010).
23. S. Fuchs, A. Rensing-Ehl, C. Speckmann, B. Bengsch, A. Schmitt-Graeff, I. Bondzio, A. Maul-Pavicic, T. Bass, T. Vraetz, B. Strahm, T. Ankermann, M. Benson, A. Caliebe, R. Fölster-Holst, P. Kaiser, R. Thimme, W. W. Schamel, K. Schwarz, S. Feske, S. Ehl, Antiviral and regulatory T cell immunity in a patient with stromal interaction molecule 1 deficiency. *J. Immunol.* **188**, 1523–1533 (2012).
24. C. Picard, C. A. McCarl, A. Papolos, S. Khalil, K. Lüthy, C. Hivroz, F. LeDeist, F. Rieux-Laucat, G. Rechavi, A. Rao, A. Fischer, S. Feske, STIM1 mutation associated with a syndrome of immunodeficiency and autoimmunity. *N. Engl. J. Med.* **360**, 1971–1980 (2009).
25. J. Böhm, F. Chevessier, A. M. De Paula, C. Koch, S. Attarian, C. Feger, D. Hantaï, P. Laforêt, K. Ghorab, J.-M. Vallat, M. Fardeau, D. Figarella-Branger, J. Pouget, N. B. Romero, M. Koch, C. Ebel, N. Levy, M. Krahn, B. Eymard, M. Bartoli, J. Laporte, Constitutive activation of the calcium sensor STIM1 causes tubular-aggregate myopathy. *Am. J. Hum. Genet.* **92**, 271–278 (2013).
26. H. Stormorken, O. Sjaastad, A. Langslet, I. Sulg, K. Egge, J. Diderichsen, A new syndrome: Thrombocytopathia, muscle fatigue, asplenia, miosis, migraine, dyslexia and ichthyosis. *Clin. Genet.* **28**, 367–374 (1985).
27. H. Stormorken, H. Holmsen, R. Sund, K. S. Sakariassen, T. Hovig, E. Jellum, N. O. Solum, Studies on the haemostatic defect in a complicated syndrome. An inverse Scott syndrome platelet membrane abnormality? *Thromb. Haemost.* **74**, 1244–1251 (1995).
28. D. Misceo, A. Holmgren, W. E. Louch, P. A. Holme, M. Mizobuchi, R. J. Morales, A. M. de Paula, A. Stray-Pedersen, R. Lyle, B. Dalhus, G. Christensen, H. Stormorken, G. E. Tjønnfjord, E. Frengen, A dominant STIM1 mutation causes Stormorken syndrome. *Hum. Mutat.* **35**, 556–564 (2014).
29. V. Nesin, G. Wiley, M. Kousi, E. C. Ong, T. Lehmann, D. J. Nicholl, M. Suri, N. Shahrizaila, N. Katsanis, P. M. Gaffney, K. J. Wierenga, L. Tsiokas, Activating mutations in STIM1 and ORAI1 cause overlapping syndromes of tubular myopathy and congenital miosis. *Proc. Natl. Acad. Sci. U.S.A.* **111**, 4197–4202 (2014).
30. G. Morin, N. O. Bruechle, A. R. Singh, C. Knopp, G. Jedraszak, M. Elbracht, D. Brémond-Gignac, K. Hartmann, H. Sevestre, P. Deutz, D. Hérent, P. Nürnberg, B. Roméo, K. Konrad, M. Mathieu-Dramard, J. Oldenburg, E. Bourges-Petit, Y. Shen, K. Zerres, H. Ouadid-Ahidouch, J. Rochette, Gain-of-function mutation in STIM1 (P.R304W) is associated with Stormorken syndrome. *Hum. Mutat.* **35**, 1221–1232 (2014).
31. C. Hedberg, M. Niceta, F. Fattori, B. Lindvall, A. Ciolfi, A. D'Amico, G. Tasca, S. Petrini, M. Tulinius, M. Tartaglia, A. Oldfors, E. Bertini, Childhood onset tubular aggregate myopathy associated with de novo STIM1 mutations. *J. Neurol.* **261**, 870–876 (2014).
32. O. Borsani, D. Piga, S. Costa, A. Govoni, F. Magri, A. Artoni, C. M. Cinnante, G. Fagiolari, P. Ciscato, M. Moggio, N. Bresolin, G. P. Comi, S. Corti, Stormorken syndrome caused by a p.R304W STIM1 mutation: The first italian patient and a review of the literature. *Front. Neurol.* **9**, 859 (2018).
33. G. Morin, V. Biancalana, A. Echaniz-Laguna, J. B. Noury, X. Lornage, M. Moggio, M. Ripolone, R. Violano, P. Marcorelles, D. Maréchal, F. Renaud, C. A. Maurage, C. Tard, J. M. Cuisset, J. Laporte, J. Böhm, Tubular aggregate myopathy and Stormorken syndrome: Mutation spectrum and genotype/phenotype correlation. *Hum. Mutat.* **41**, 17–37 (2020).
34. T. H. Gamage, G. Gunnes, R. H. Lee, W. E. Louch, A. Holmgren, J. D. Bruton, E. Lengle, T. R. S. Kolstad, T. Revold, S. S. Amundsen, K. T. Dalen, P. A. Holme, G. E. Tjønnfjord, G. Christensen, H. Westerblad, A. Klungland, W. Bergmeier, D. Misceo, E. Frengen, STIM1 R304W causes muscle degeneration and impaired platelet activation in mice. *Cell Calcium* **76**, 87–100 (2018).
35. T. H. Gamage, E. Lengle, G. Gunnes, H. Pullisaar, A. Holmgren, J. E. Reseland, E. Merckoll, S. Corti, M. Mizobuchi, R. J. Morales, L. Tsiokas, G. E. Tjønnfjord, R. S. Lacruz, S. P. Lyngstadaas, D. Misceo, E. Frengen, STIM1 R304W in mice causes subgingival hair growth and an increased fraction of trabecular bone. *Cell Calcium* **85**, 102110 (2020).
36. R. Silva-Rojas, S. Treves, H. Jacobs, P. Kessler, N. Messaddeq, J. Laporte, J. Böhm, STIM1 over-activation generates a multi-systemic phenotype affecting skeletal muscle, spleen, eye, skin, bones, and the immune system in mice. *Hum. Mol. Genet.* **15**, 1579–1593 (2019).
37. I. Brandsma, D. C. Gent, Pathway choice in DNA double strand break repair: Observations of a balancing act. *Genome Integr.* **3**, 9 (2012).
38. P. Rathner, M. Stadlbauer, C. Romanin, M. Fahrner, I. Derler, N. Müller, Rapid NMR-scale purification of ^{15}N,^{13}C isotope-labeled recombinant human STIM1 coiled coil fragments. *Protein Expr. Purif.* **146**, 45–50 (2018).
39. A. G. Palmer III, Nmr probes of molecular dynamics: Overview and comparison with other techniques. *Annu. Rev. Biophys. Biomol. Struct.* **30**, 129–155 (2001).
40. G. N. Ramachandran, C. Ramakrishnan, V. Sasisekharan, Stereochemistry of polypeptide chain configurations. *J. Mol. Biol.* **7**, 95–99 (1963).
41. S. van Dorp, R. Qiu, U. B. Choi, M. M. Wu, M. Yen, M. Kirmiz, A. T. Brunger, R. S. Lewis, Conformational dynamics of auto-inhibition in the ER calcium sensor STIM1. *Elife* **10**, e66194 (2021).
42. H. M. Strauss, S. Keller, Pharmacological interference with protein-protein interactions mediated by coiled-coil motifs. *Handb. Exp. Pharmacol.* **186**, 461–482 (2008).
43. I. Derler, M. Hofbauer, H. Kahr, R. Fritsch, M. Muik, K. Kepplinger, M. E. Hack, S. Moritz, R. Schindl, K. Groschner, C. Romanin, Dynamic but not constitutive association of calmodulin with rat TRPV6 channels enables fine tuning of $Ca2^+$–dependent inactivation. *J. Physiol.* **577**, 31–44 (2006).
44. T. Zal, N. R. Gascoigne, Photobleaching-corrected FRET efficiency imaging of live cells. *Biophys. J.* **86**, 3923–3939 (2004).
45. D. Bashford, Macroscopic electrostatic models for protonation states in proteins. *Front. Biosci.* **9**, 1082–1099 (2004).
46. G. Kieseritzky, E. W. Knapp, Optimizing pKA computation in proteins with pH adapted conformations. *Proteins* **71**, 1335–1348 (2008).
47. M. L. Connolly, Analytical molecular surface calculation. *J. Appl. Cryst.* **16**, 548–558 (1983).
48. B. Rabenstein, E. W. Knapp, Calculated pH-dependent population and protonation of carbon-monoxy-myoglobin conformers. *Biophys. J.* **80**, 1141–1150 (2001).
49. S. Jo, T. Kim, V. G. Iyer, W. Im, CHARMM-GUI: A web-based graphical user interface for CHARMM. *J. Comput. Chem.* **29**, 1859–1865 (2008).
50. J. Lee, X. Cheng, J. M. Swails, M. S. Yeom, P. K. Eastman, J. A. Lemkul, S. Wei, J. Buckner, J. C. Jeong, Y. Qi, S. Jo, V. S. Pande, D. A. Case, C. L. Brooks III, A. D. MacKerell Jr., J. B. Klauda, W. Im, CHARMM-GUI input generator for NAMD, GROMACS, AMBER, OpenMM, and CHARMM/OpenMM simulations using the CHARMM36 additive force field. *J. Chem. Theory Comput.* **12**, 405–413 (2016).
51. E. F. Pettersen, T. D. Goddard, C. C. Huang, G. S. Couch, D. M. Greenblatt, E. C. Meng, T. E. Ferrin, UCSF Chimera--A visualization system for exploratory research and analysis. *J. Comput. Chem.* **25**, 1605–1612 (2004).
52. J. Schlitter, M. Engels, P. Krüger, Targeted molecular dynamics: A new approach for searching pathways of conformational transitions. *J. Mol. Graph.* **12**, 84–89 (1994).
53. J. C. Phillips, R. Braun, W. Wang, J. Gumbart, E. Tajkhorshid, E. Villa, C. Chipot, R. D. Skeel, L. Kalé, K. Schulten, Scalable molecular dynamics with NAMD. *J. Comput. Chem.* **26**, 1781–1802 (2005).
54. J. Huang, S. Rauscher, G. Nawrocki, T. Ran, M. Feig, B. L. de Groot, H. Grubmüller, A. D. MacKerell Jr., CHARMM36m: An improved force field for folded and intrinsically disordered proteins. *Nat. Methods* **14**, 71–73 (2017).
55. D. R. Roe, T. E. Cheatham III, PTRAJ and CPPTRAJ: Software for processing and analysis of molecular dynamics trajectory data. *J. Chem. Theory Comput.* **9**, 3084–3095 (2013).
56. H. T. Nguyen, S. A. Pabit, L. Pollack, D. A. Case, Extracting water and ion distributions from solution x-ray scattering experiments. *J. Chem. Phys.* **144**, 214105 (2016).
57. R. T. McGibbon, K. A. Beauchamp, M. P. Harrigan, C. Klein, J. M. Swails, C. X. Hernández, C. R. Schwantes, L. P. Wang, T. J. Lane, V. S. Pande, MDTraj: A modern open library for the analysis of molecular dynamics trajectories. *Biophys. J.* **109**, 1528–1532 (2015).
58. O. Sercinoglu, P. Ozbek, gRINN: A tool for calculation of residue interaction energies and protein energy network analysis of molecular dynamics simulations. *Nucleic Acids Res.* **46**, W554–W562 (2018).
59. A. Barducci, G. Bussi, M. Parrinello, Well-tempered metadynamics: A smoothly converging and tunable free-energy method. *Phys. Rev. Lett.* **100**, 020603 (2008).
60. G. Bussi, A. Laio, Using metadynamics to explore complex free-energy landscapes. *Nat. Rev. Phys.* **2**, 200–212 (2020).

61. G. Fiorin, M. L. Klein, J. Hénin, Using collective variables to drive molecular dynamics simulations. *Molecular Physics* **111**, 3345–3362 (2013).
62. T. M. Schafer, G. Settanni, Data reweighting in metadynamics simulations. *J. Chem. Theory Comput.* **16**, 2042–2052 (2020).

Acknowledgments: We thank A. Klungland and H. C. Aas at Oslo University Hospital (OUH) for valuable input to the project and technical assistance. We acknowledge the assistance from the Norwegian Transgenic center (University of Oslo) in establishing the mouse line and the Department of Comparative Medicine (OUH) for assistance and technical support in handling and maintenance of the mouse colony. We thank S. Buchegger for supporting cell culture and transfection. The artwork in Fig. 6 was supported by B. Belohlavy. **Funding:** T.H.G. was supported financially by the Quota scheme of Norwegian State Educational Loan Fund, "Foundation in support of study stays abroad for fellows and younger medical researchers at the Faculty of Medicine" and through "Mobility grant for PhD students at the Institute for Clinical medicine," University of Oslo. H.G. and F.H. hold PhD scholarships of the Austrian Science Fund (FWF) PhD program W1250 "NanoCell". NMR measurements were supported by the "iNEXT" infrastructure project (PID: 6162), which is funded by the Horizon 2020 programme of the European Commission and by the EFRE INTERREG IV ETC-AT-CZ program (project id M00146 "RERI- uasb") of the European Union. Additional funding was provided by Austrian Science Fund (FWF) P32947 to M.F. and P32778, P33283, and P34884 to C.R. **Author contributions:** E.F. and C.R. conceived and oversaw the project. T.H.G., M.F., H.G., and F.H. designed the study and drafted the manuscript. T.H.G., D.M., W.E.L., G.G., H.P., J.E.R., S.P.L., A.H., and S.S.A. conducted animal experiments, phenotyping, and data analyses. M.F. carried out molecular biology experiments. P.R., L.C., E.R., C.L., and N.M. conducted and analyzed NMR experiments. H.G. performed and analyzed electrophysiological and fluorescence microscopy experiments. F.H., H.K., and T.R. carried out MD simulations. All authors reviewed and approved the final version of the manuscript. **Competing interests:** The authors declare that they have no competing interests. **Data and materials availability:** All data needed to evaluate the conclusions in the paper are present in the paper or the Supplementary Materials. Cell and tissue samples from the double-mutant Stim1 E296del+R304W mice are available from E.F. under a material transfer agreement with the University of Oslo.

Submitted 17 May 2022
Accepted 18 January 2023
Published 7 February 2023
10.1126/scisignal.add0509